Analysis of two-photon photoemission from Si(001)

H. Husser* and E. Pehlke

Institut für Theoretische Physik und Astrophysik, Christian-Albrechts-Universität Kiel, 24098 Kiel, Germany

(Received 20 September 2012; published 19 December 2012)

We have applied our *ab initio* simulation approach for the photoemission process at solid surfaces to calculate two-photon photoemission spectra from the $p(2 \times 2)$-reconstructed Si(001) surface. In this approach, the ground-state electronic structure of the surface is obtained within density functional theory. The subsequent time-dependent simulation is carried through at frozen effective potential, while an optical potential is applied to account for inelastic scattering in the excited state. We have derived normal emission spectra for s- and p-polarized light with photon energies in the range $\hbar\omega = 3.85$–4.75 eV. The dependence of the theoretical spectra on photon energy and polarization is analyzed and compared to experimental spectra from the literature. To unravel the role of the unoccupied states between Fermi energy and the vacuum level which are acting as intermediate states in the excitation process, we investigate the expression for the two-photon photocurrent from perturbation theory. The scattering states, which serve as the final states of photoemission, are obtained from a time-dependent simulation of a LEED-type experiment. The evaluation of the dipole matrix elements allows us to identify the relevant bulk band transitions and to address the influence of surface states.

DOI: 10.1103/PhysRevB.86.235134 PACS number(s): 79.60.−i, 73.20.At

I. INTRODUCTION

Two-photon photoemission (2PPE) spectroscopy is widely used to probe the energetics and dynamics of the unoccupied electronic states at solid surfaces, thin films, and nanostructures.[1] The development over the last decades has been facilitated by advances in ultrafast laser techniques and high-resolution electron analyzers.[2] The unoccupied electronic states (conduction bands) are of considerable interest due to their decisive role in excitation, relaxation, chemical, and transport processes. Time-resolved 2PPE pump-probe spectroscopy allows one to follow such dynamical processes directly on a femtosecond timescale. In particular, it can be used to extract information about the lifetime of electronic excitations.[2,3]

The 2PPE process can be thought of as two photon-induced resonant or nonresonant excitation steps.[3] The first one promotes the system into an excited electronic state, the so-called intermediate state; in the second step, an electron is lifted above the vacuum level into the final state. Thus, at the same time the occupied and unoccupied (valence and conduction) states are probed and can give rise to features in the spectra. Frequently, the origin of the peaks can be identified by their dispersion with photon energy. However, the interpretation of 2PPE spectra can become complicated in case of interfering excitation paths. Furthermore, scattering of electrons can occur in the excited state which results in a depopulation and population dynamics of the intermediate states involved in the scattering. In a time-resolved experiment, scattering rates of excited electrons can be obtained from the variation of peak intensities with the time delay between pump and probe pulse.

Early 2PPE pump-probe studies have addressed the hot bulk carrier dynamics in semiconductors and the thermalization of photogenerated nonequilibrium electron distributions in laser-heated metals.[4–8] Beside the bulk excited-state population dynamics, the long-lived image-potential states (IPS) in front of metal surfaces[9,10] have been studied intensely with 2PPE.[11–19] These states have proven to be sensitive probes for the surface morphology and adsorbate-induced modifications at surfaces.[20–28] Electrons in IPS can undergo localization via polaron formation and solvation at metal-polar adsorbate interfaces.[29–33] The coupling of excited electrons to the nuclear degrees of freedom is investigated in surface femtochemistry, with the goal of laser-control of chemical reactions.[1,34,35] Image states can also be employed as probes for the spin-dependent electronic structure, and spin-resolved 2PPE has been introduced to follow the electron relaxation dynamics in ferromagnetic systems and spintronic devices.[36–45] By now, the field of application for 2PPE pump-probe spectroscopy has been extended to the high-T_C superconducting cuprates,[46–48] to other ordered states such as charge density waves and phase (metal-insulator) transitions,[49–52] and, most recently, also to topological insulators.[53]

Quantum interference in the excited state has been demonstrated by the coherent excitation of electron wave packets into the Rydberg series of IPS in front of metal surfaces leading to quantum beat patterns in the spectra.[54–56] The possibility of optical phase control of electrons[57–59] and coherently controlled electrical currents[60] has been shown stressing the importance of quantum mechanical phase in 2PPE.

Considerable progress has been made in the identification of the different processes that lead to the decay of the laser-created population in the excited state.[61–73] Inelastic lifetimes due to electron-electron scattering can be obtained from quasiparticle self-energy calculations, usually within the *GW* approximation.[70,74–77] Direct simulations of the evolution of photoexcited electron distributions in time-resolved 2PPE have been performed in the framework of density matrix theory.[78–82] Elaborate models have been set up to include competing deexcitation processes via scattering with electrons and phonons and (ballistic) transport on a microscopic, quantum-mechanical level. An essential understanding of how energy relaxation and dephasing times are linked to observed linewidths and cross-correlation traces (2PPE signal as a function of pump-probe delay) can readily be gained by solving the optical Bloch equations for model systems with only a few electronic levels.[3,16,83] The elastic and inelastic scattering rates enter as phenomenological parameters. On a fundamental level of theory, nonequilibrium Green's functions have been used to

investigate the effect of Coulomb interactions and in particular the importance of hole scattering in the time-resolved 2PPE process.[84–86]

Besides the description of the basic physical mechanisms there is a need for quantitative computational schemes taking full account of the band structure of the material in order to be able to compare to 2PPE experiments. Especially, this should be helpful to explore the possibility of mapping unoccupied bulk band structures via 2PPE; see in particular Refs. 87 and 88.

In the present paper we apply a general approach developed for the direct simulation of photoexcitation and the photoemission process at solid surfaces. It is based on time-dependent density functional theory (TDDFT) and allows us to calculate high-order photoemission currents including and beyond two-photon processes. We have derived 2PPE normal emission spectra from the Si(001) surface excited by a single coherent femtosecond laser pulse. A comparison to experimental spectra by Shudo and Munakata[89] and by Kentsch *et al.*[90] is presented. The spectra are analyzed using the perturbation series expansion for the 2PPE currents with respect to the external potential in order to identify the contributions from different intermediate states.

Among the semiconductor surfaces the Si(001) surface has been subject of detailed investigation by 2PPE. The existence of image states and the formation of long-lived excitons have been demonstrated.[91,92] Different relaxation mechanisms of the photoexcited carriers that rely on the bulk and surface band structures have been elucidated.[93–97] Moreover, the Si(001) surface is one of the few examples where, at the present time, detailed information on the conduction bulk band structure has been extracted via 2PPE.[89,90] Only recently, Si(001) has found new interest when the existence of Fano-type line profiles in 2PPE due to interference between surface resonances and the substrate continuum has been shown[98] and when a surface resonance within the energy range of the conduction bands has been identified.[99]

The outline of the paper is as follows. In Sec. II A, we summarize the direct simulation approach to photoemission from solid surfaces, i.e., the equations of motions and the procedure to calculate angle-resolved spectra. Computational details are given in Sec. II B. Before we present calculated normal emission 2PPE spectra from the Si(001)$p(2 \times 2)$ surface in response to a single fs laser pulse (i.e., no pump-probe simulation) in Sec. III A, we compile the dipole selection rules based on the perturbation expansion for the photocurrents in Sec. II C. The spectra are analyzed with respect to initial-state contributions in Sec. III B and compared to experimental spectra from the literature in Sec. III C. Following some general considerations in Sec. IV A, the role of intermediate states in the origin of the spectral peaks is investigated in Sec. IV B. The surface-projected density of the unoccupied states and a further discussion of intermediate states can be found in the appendices. We conclude the paper with a summary in Sec. V.

II. THEORY

A. The direct simulation of photoemission from solid surfaces

We have described our method for the real-time simulation of the photoemission process from solid surfaces, clusters, or molecules within the framework of TDDFT in Ref. 100, to which we refer the reader for details. Here we give a brief outline of the main features including the simulation geometry, the time-dependent equations, and the derivation of the photoemission spectra.

The photoexcitation of the surface induced by a femtosecond laser pulse is simulated within a repeated-slab geometry to which absorbing boundary conditions are imposed. Each supercell comprises a surface slab together with a sufficiently large vacuum region for the real-space propagation of the photoemitted electrons. An absorptive potential confined to a thin slab and placed in mid-vacuum is used to electronically decouple neighboring slabs. The photocurrents that pass through a cross-section area of the supercell are integrated in order to obtain the photoemission spectra.

The equilibrium atomic configuration and ground-state electronic density of the surface, which is taken as the initial state before the external perturbation is switched on, are obtained from a density functional calculation.[101] A local approximation to the exchange-correlation (xc) functional is employed, and the ion cores are described by pseudopotentials. Parameters of our computation are given in Sec. II B.

The time-dependent electric field $\mathbf{E}$ of the laser pulse is described within the dipole approximation by a spatially homogeneous, time-dependent vector potential,

$$\mathbf{A}(t) = -c \int_{-\infty}^{t} dt' \mathbf{E}(t'), \quad \Phi(t) \equiv 0. \tag{1}$$

With this choice of gauge the time-dependent Hamiltonian maintains the lattice periodicity of the ground state which is crucial for our setup. Using a vector potential entails, however, the necessity of adding gauge-dependent terms to the nonlocal operators.

The Kohn-Sham equations of motion for the time evolution of the electronic system,

$$i \frac{\partial \psi(t)}{\partial t} = \hat{H}_{KS}^{(\mathbf{A})}(t) \psi(t), \tag{2}$$

are integrated for frozen atomic positions $\mathbf{R}_i$ and frozen ground-state electron density $n_0(\mathbf{r})$ in this work. Thus, in the Hamiltonian

$$\hat{H}_{\mathrm{KS}}^{(\mathbf{A})}(t) = \frac{1}{2}\left(\hat{\mathbf{p}} + \frac{\mathbf{A}(t)}{c}\right)^2 + \hat{V}_{\mathrm{eff,loc}} + \hat{V}_{\mathrm{ps,nl}}^{(\mathbf{A})} + \hat{V}_{\mathrm{opt}}^{(\mathbf{A})}, \tag{3}$$

the local part $\hat{V}_{\mathrm{eff,loc}}$ of the effective potential, which comprises the Hartree potential, the xc potential, and the local part of the pseudopotentials, is time independent. This corresponds to the approximation of a single active electron moving in the ground-state effective potential. The extension to TDDFT molecular dynamics, that is, to time-dependent effective potentials and to ions that are allowed to move, has been briefly addressed in Ref. 100.

While the effective potential is kept frozen to its ground-state value, the optical-potential operator $\hat{V}_{\mathrm{opt}}^{(\mathbf{A})}$ roughly accounts for the inelastic scattering events experienced by the excited electrons within the crystal. This operator serves as an approximation to the complex self-energy $\hat{\Sigma}$ of the excited quasiparticle states. The restriction to the excited-state admixtures of the time-dependent wave functions is ensured by projecting onto the conduction band states. In this way, the

optical potential becomes a nonlocal operator even if a local approximation for $\hat{\Sigma}$ is used.

Finally, $V_{\mathrm{ps,nl}}^{(\mathbf{A})}$ denotes the nonlocal part of the pseudopotentials which we use in the fully separable Kleinman-Bylander form.[102] The superscripts (**A**) at the nonlocal operators refer to the applied gauge. All nonlocal potentials carry a time-dependent phase factor[103] that follows from the gauge transform of the wave functions.[104]

The total time-dependent photocurrent density at some height z above the sample surface is obtained by summing the contributions from the Kohn-Sham wave functions of all initially occupied states. In the computation of the spectrally resolved photocurrents, an intermediate step is taken that consists in transforming the electronic wave functions to the rest frame of the oscillating electrons (Kramers-Henneberger transform; see, e.g., Ref. 105). In this frame of reference the external electric field vanishes so that the electrons emitted into the vacuum region propagate like free particles. The effect of the electron detector, selecting energy (ε) and emission angles (ϑ and φ) in experiment, is accounted for by applying suitably defined projection operators to the wave functions. The photoemitted charge per unit cell and femtosecond laser pulse follows from the integration of the energy- and angle-resolved photocurrent density over both time and a cross-section area of the slab. The resulting expression for normal emission as applied in this work can be found in Ref. 100.

B. The Si(001) surface and computational parameters

Figure 1 shows a schematic top and side view of the $p(2 \times 2)$ reconstructed Si(001) surface which, for simplicity, has been assumed for all calculations in this work. The dimerization of neighboring silicon atoms in the topmost layer saturates half of the broken bonds of the unreconstructed surface giving rise to the basic (2×1) reconstruction.[106] A further reduction of the surface energy is achieved by tilting the silicon dimers[107,108] as shown in the lower panel of Fig. 1. The $p(2 \times 2)$ reconstruction arises when the sign of the buckling angle alternates along the dimer rows. It differs from the (ground-state) $c(4 \times 2)$ reconstruction only in the relative phase of the dimer buckling in adjacent rows. From the remaining dangling bonds at the two Si-up and Si-down atoms per unit cell two occupied ($D_{\mathrm{up}}, D'_{\mathrm{up}}$) and two unoccupied ($D_{\mathrm{down}}, D'_{\mathrm{down}}$) surface state bands are formed. Parts of these bands fall into the energy gap between the valence and the conduction states in the projected bulk band structure.[109–111] Dangling bond states at $\bar{\Gamma}$ are displayed in the lower panel of Fig. 1. These states constitute the most prominent surface states of the Si(001) surface.

The relaxation of the geometric and electronic surface structure has been performed with the DFT code FHI96MD.[101] The local density approximation (LDA) is applied to the xc energy functional. In case of the ground-state calculation, the **k**-point set for the approximate Brillouin zone integrations comprises 9 special wave vectors in the irreducible part of the Brillouin zone, while in the subsequent non-self-consistent time-dependent simulation only the wave functions at $\bar{\Gamma}$ are considered. The basis set for the expansion of the wave functions is composed of plane waves up to an energy cutoff of 10 Ry. The surface slabs consist of 36 silicon layers which corresponds to a total thickness of about $90a_0$. The bottom

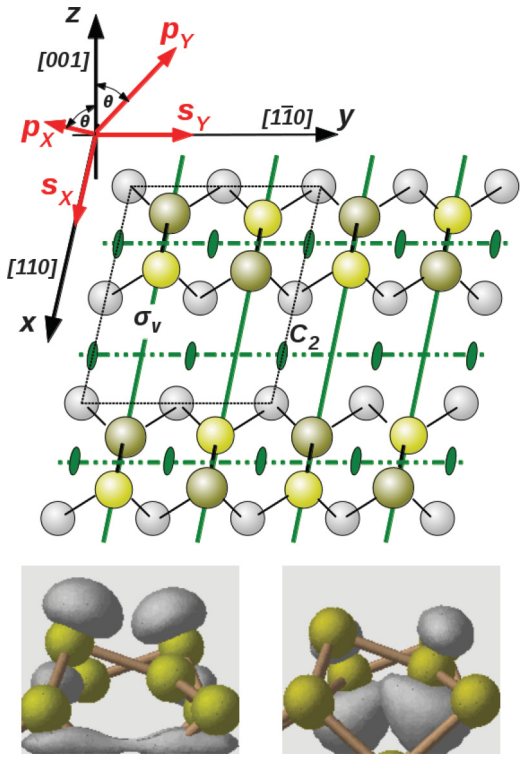

FIG. 1. (Color online) Sketch of the reconstruction geometry and the symmetry elements of the Si(001) $p(2 \times 2)$ surface. Upper panel: Top view. Top-layer Si atoms are denoted by shaded spheres. Darker and lighter shade denotes the atoms of the Si dimer that have relaxed outwards (Si-up atoms) or inwards (Si-down atoms), respectively. The thin line frames the $p(2 \times 2)$ surface unit cell. Mirror planes perpendicular to the surface (σ_v) and glide planes are indicated by solid lines and dash-dotted lines, respectively. C_2 denotes the twofold rotational axes. The coordinate axes point along the direction of the dimer bonds (x), dimer rows (y), and the surface normal (z). The photoemission geometry for a single-domain surface is indicated in addition. The direction of the polarization vector of the incident s- and p-polarized light wave is chosen along the directions marked by the arrows (denoted by s_X, s_Y, p_X, and p_Y). Lower panel: Side view. Buckling of the silicon dimers in the topmost layer and the back bonds to the atoms of the second layer. The left and right parts show a contour surface of the occupied (D_{up}) and unoccupied (D_{down}) dangling bond states at $\bar{\Gamma}$, respectively.

side of the slab is passivated by hydrogen atoms. Neighboring slabs are separated by a vacuum region of about $60a_0$. The parameters required for converged Si(001) photoemission spectra have been established in Ref. 100.

The scheme for the integration of the time-dependent Kohn-Sham equations is described in Ref. 112. For the calculation of normal emission spectra, the time propagation has been restricted to wave functions at $\bar{\Gamma}$. A complex absorptive potential of $8a_0$ extension, placed in mid-vacuum, is used to electronically decouple neighboring slabs in the time-dependent simulation. The same potential as in Ref. 100 is employed in this work.

We apply a single coherent laser pulse of center frequency ω with an envelope function of Gaussian shape for the excitation of the surface. The photon energies, chosen in the range $\omega = 3.85$–4.75 eV, are kept below the ionization energy of

$\xi \approx 5.4$ eV.[90] If the band gap correction is taken into account, this value of ξ coincides with the ionization energy of the slab in our simulations. The width $\Delta t_p = 10$ fs of the Gaussian envelope of the laser pulse corresponds to an energy resolution of $\Delta\omega = 65$ meV. However, in order to avoid artifacts due to the discrete spectrum of a slab with finite thickness, the spectra have further been convoluted with a Gaussian (of 112.5 meV width) resulting in a resolution of $\Delta\varepsilon = 130$ meV. The total simulation time of 70 fs exceeds the total pulse duration of $2t_p = 55$ fs (at this point the pulse is switched off) by an amount that is sufficient to collect all photoelectrons. The maximum electrical field strength of $E_0 \approx 8 \times 10^{-3}$ H/$a_0 \approx 0.4$ V/Å is tantamount to a peak intensity of $I \approx 2.25 \times 10^{12}$ W/cm^2. This is sufficient to yield reliable 2PPE photocurrents; on the other hand it remains in the range where the 2PPE part of the spectrum scales quadratically with photon intensity.

The optical potential (self-energy) is approximated by a complex energy-independent constant which is acting to shift and damp both the intermediate and final states of the 2PPE process. These states cover the range from 1 eV to 10 eV above the valence band maximum (VBM). Following the quasiparticle self-energy corrections to the Kohn-Sham eigenenergies for Si as calculated within the *GW* approximation by Fleszar and Hanke,[113] we have chosen an average value of $\mathrm{Im}(v_{\mathrm{opt}}) \approx 0.5$ eV for the imaginary part of the optical potential. This choice reflects the scattering of electrons about 10 eV above the VBM which corresponds to the final state energy of the photoemitted electrons. Its value is larger than the value derived from the self energy of Si at the eigenenergies of the intermediate states. The imaginary part of v_{opt} is set constant within the slab and decays proportional to the electronic ground-state density into the vacuum region. Furthermore, a spatially constant real part is added to v_{opt}. It acts on the band structure like a scissor operator and is included to account for the LDA band gap correction of $\mathrm{Re}(v_{\mathrm{opt}}) \approx 0.6$ eV (value taken from the same Ref. 113).

C. Perturbational expansion of the photocurrent—symmetry selection rules for 2PPE in normal emission

Symmetry selection rules constitute an important tool for the analysis of photoemission spectra, in particular if the incident light has a certain polarization of well-defined symmetry (see, e.g., Ref. 114 for the case of 2PPE). In this section we summarize the 2PPE dipole selection rules for the Si(001)$p(2\times2)$ surface which follow from the perturbation expansion of the photocurrent. The two-dimensional symmetry group of the $p(2\times2)$ surface and the dipole selection rules for one-photon photoemission (1PPE) in normal emission have been explicated in Ref. 100. The group of the wave vector $\bar{\Gamma}$ is C_{2v}. Its four one-dimensional irreducible representations[115] are listed in Table I.

The 2PPE photocurrent can, in principle, be calculated from a perturbation expansion with respect to the vector potential $\hat{\mathbf{A}}$ associated with the external field (see Ref. 87),

$$j_{\mathbf{R}}(\varepsilon) \propto \frac{v}{R^2} \sum_i^{\mathrm{occ}} \left| \sum_m \frac{\langle \phi^*_{\mathrm{LEED}} | \hat{O} | m \rangle \langle m | \hat{O} | i \rangle}{\varepsilon_i - \varepsilon_m + \omega + i\eta_m} \right|^2 \delta(\varepsilon - \varepsilon_i - 2\omega). \tag{4}$$

TABLE I. Characters of the irreducible representations of the symmetry group C_{2v}. The symmetry elements are depicted in Fig. 1. If the polarization vector of the electric field points into one of the coordinate directions (x, y, or z, listed in the second column), the dipole operator transforms according to the irreducible representation in the same line.

$\mathbf{C}_{2v}$		E	C_2	σ_v	σ'_v
A_1	z	1	1	1	1
A_2	(xy)	1	1	−1	−1
B_1	x	1	−1	1	−1
B_2	y	1	−1	−1	1

Here, $j_{\mathbf{R}}(\varepsilon)$ denotes the current of outgoing photoelectrons with energy ε and velocity v as measured by a detector placed at position $\mathbf{R}$ far outside the sample (the surface is located at $z = 0$). $\hat{O}$ is the dipole operator $\hat{O} = \frac{1}{2c}(\hat{\mathbf{p}} \cdot \hat{\mathbf{A}} + \hat{\mathbf{A}} \cdot \hat{\mathbf{p}}) = \hat{\mathbf{p}} \cdot \hat{\mathbf{A}}/c$ (since $[\hat{\mathbf{p}}, \hat{\mathbf{A}}] = 0$ in dipole approximation), and $\mathbf{A}$ denotes the amplitude.[116] The eigenstates $|i\rangle$ and $|m\rangle$ refer to the initial and intermediate states with energies ε_i and ε_m, respectively. The energies ε_m in Eq. (4) are shifted by $\mathrm{Re}(v_{\mathrm{opt}})$, so that the band gap correction is accounted for. The values $-i\eta_m$ denote the finite imaginary part of the self-energy. The final states $|f\rangle \equiv |\phi^*_{\mathrm{LEED}}\rangle$ are taken to be time-reversed LEED states as are usually employed in the one-step model of 1PPE.[117] They inherently contain the emission direction and account for the multiple scattering of the photoelectron in the surface region as well as in the bulk. The above expression is written with effective one-electron states that are eigenstates of the unperturbed single-particle Hamiltonian $\hat{H}_0$. Equation (4) is valid for a continuous wave with a photon energy ω below the ionization energy. Energy conservation for the 2PPE process as a whole is ensured by the δ function. In the case of a finite laser pulse, the most simple approximation is given by the convolution with the spectral shape of the pulse. Some of the general features of expression (4) will be analyzed further in Sec. IV.

Equation (4) shows that each of the two electronic transitions caused by the external field—the first one leading from the initial state (IS) to the intermediate state (IMS), the second one from the intermediate to the final state (FS)—obeys a selection rule. Assuming linearly polarized light in dipole approximation and splitting the vector potential into Cartesian components, $\mathbf{A} = \sum_j A_j \hat{\mathbf{e}}_j$, the product of matrix elements in the numerators of Eq. (4) take the form

$$\langle f | \hat{\mathbf{p}} \cdot \hat{\mathbf{A}} | m \rangle \langle m | \hat{\mathbf{p}} \cdot \hat{\mathbf{A}} | i \rangle = \sum_j \sum_k A_j A_k \langle f | \hat{p}_j | m \rangle \langle m | \hat{p}_k | i \rangle. \tag{5}$$

In the case of normal emission, the FS $|f\rangle$ describing the outgoing photoelectron is A_1 symmetric. Hence the product of the matrix elements does not vanish only if the IMS transforms according to the same irreducible representation as the momentum operator component $\hat{p}_j$, and if the IS belongs to the same (irreducible) representation as the product of $|m\rangle$ and $\hat{p}_k$. Analyzing Eq. (5) for the possible polarizations of the external field, one obtains the selection rules of Table II, in which the allowed excitation paths "IS → IMS → FS" for normal emission 2PPE are listed.

TABLE II. Allowed symmetries of the initial and intermediate states and electric fields inducing the associated transitions in normal emission 2PPE for the symmetry group C_{2v}. In the first column for the applied external field components, an entry such as $x\&y$ denotes a polarization vector that lies in the x-y plane but is not parallel to either of the coordinate axes. In this case, only the additional transitions are listed that require both Cartesian field components—one for the first, the other for the second transition.

Field comp.	Type of polarization	IS	Field for $i \to m$	IMS	Field for $m \to f$	FS
x	$s_X\&p_X$	A_1	x	B_1	x	A_1
y	$s_Y\&p_Y$	A_1	y	B_2	y	
z	$p_X\&p_Y$	A_1	z	A_1	z	
$x\&y$	$s\&p$	A_2	x	B_2	y	A_1
		A_2	y	B_1	x	
$x\&z$	p_X	B_1	z	B_1	x	
		B_1	x	A_1	z	
$y\&z$	p_Y	B_2	z	B_2	y	
		B_2	y	A_1	z	

For the discussion of the Si(001) spectra in the following section we note that for s-polarized light with the electric field vector either parallel (s_Y) or perpendicular (s_X) to the dimer rows, only IS of A_1 symmetry can contribute. The IMS involved must transform according to the same irreducible representation as the dipole operator (B_2 or B_1; first two lines of Table II). Thus, differences between the s_X- and s_Y-polarized spectra (spectra for the single-domain surface) must be due to differences between the IMS of symmetries B_1 and B_2.

In p-polarized light, by contrast, there exists an additional excitation channel for the IS of A_1 symmetry via an IMS of symmetry A_1 where both transitions are caused by the z-component of the field (third line of Table II). This facilitates studying the interplay of the two kind of IMS (A_1 with B_1 in p_X-polarized light or A_1 with B_2 in p_Y-polarized light, respectively). In particular, if the total laser intensity is assumed to be the same for both s- and p-polarized light with angle of incidence $\theta = 45^\circ$, the in-surface-plane component of the field is weaker by a factor $1/\sqrt{2}$ in p-polarized light, and the associated contributions to the photocurrent are reduced by a factor 4; that is, $I_s/I_p = 4$. Thus, for IS of A_1 symmetry, deviations from this intensity ratio must be due to the presence of IMS of A_1 symmetry that are reached by virtue of the surface-normal component.

Furthermore, in p-polarized light, the first and second transition may be caused by *different* components of the external field (x & z or y & z), so that additional IS of symmetries B_1 or B_2 become accessible. Also for these IS there are two different excitation channels depending on the sequence of the actions of the two field components; see the corresponding lines in Table II. Whenever different IMS are available and yield contributions of comparable magnitude, these contributions have to be summed coherently; that is, their relative phases have to be taken into account.

For the sake of completeness we note that, in normal emission 2PPE, IMS of symmetry A_2 are forbidden, whereas IS of A_2 symmetry are only seen if the polarization vector contains nonvanishing x *and* y components. Such types of polarizations are not applied in this work.

III. SI(001) 2PPE SPECTRA AT NORMAL EMISSION

A. Overview

Normal-emission spectra, calculated for s- and p-polarized light of equal intensity and for different photon energies in the range $\hbar\omega = 3.85$–4.75 eV, are displayed in Figs. 2 and 3. The angle of incidence of the p-polarized light is $\theta = 45^\circ$. In the calculation, the plane of incidence is parallel or perpendicular to the direction of the dimer rows. All spectra have been averaged over the two directions of dimerization to account for the two-domain Si(001)$p(2 \times 2)$ surface. The spectra have been decomposed into contributions from different IS (Figs. 5 and 6). Peak positions from these individual contributions have been marked in Figs. 2 and 3. Details will be given below.

The calculated spectra can be compared to experimental Si(001) normal-emission 2PPE spectra from the literature. The spectra of Shudo and Munakata[89] comprise photon energies in the range $\hbar\omega = 3.75$–4.50 eV. The higher energy range $\hbar\omega = 4.46$–4.74 eV is covered by the spectra of Kentsch *et al.*[90]

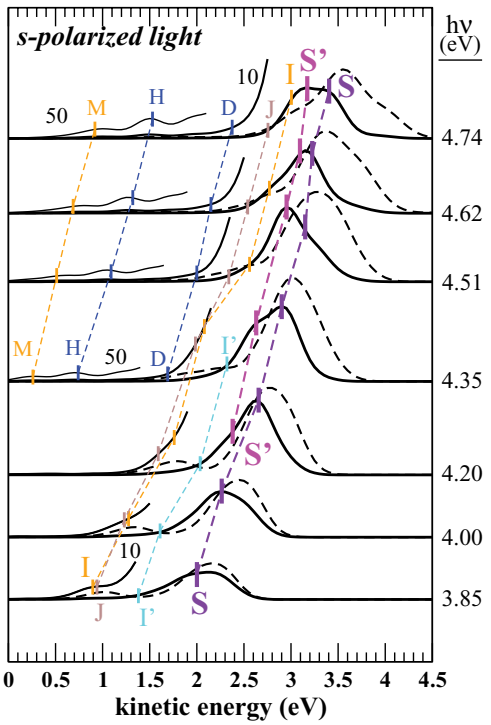

FIG. 2. (Color online) Calculated 2PPE normal emission spectra from the Si(001)$p(2 \times 2)$ surface for s-polarized light and several photon energies $h\nu$. The photocurrents have been averaged with respect to the (1×2) and (2×1) domains, with the plane of incidence being either parallel or perpendicular to the direction of the dimer rows. For comparison, the p-polarized spectra of Fig. 3 are shown by dashed lines. Parts of the spectra have been multiplied with magnification factors ($\times 10$, $\times 50$) as specified in the figure. Identifications of contributions to the spectra refer to s polarization (see Fig. 5).

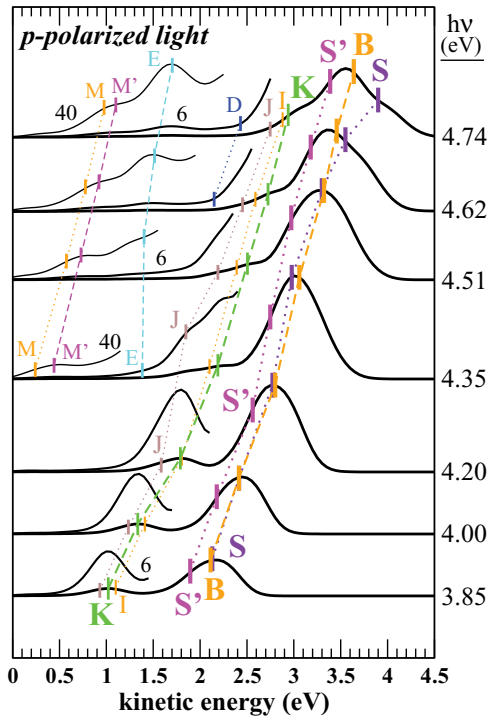

FIG. 3. (Color online) Same as Fig. 2 but for p-polarized light (of the same intensity) incident under an angle $\theta = 45°$. Magnification factors ($\times 6, \times 40$) have been applied as specified in the figure. For the identification of the contributions see Fig. 6.

These spectra are reprinted in Fig. 4. We will give a detailed comparison to the experimental spectra in Sec. III C.

The first step in the analysis of the calculated spectra consists in the decomposition into contributions arising from different initial states and specific polarizations of the light. For both s- and p-polarized light, single-domain spectra with the plane of incidence containing either the direction of the dimer rows or the direction of the dimer bonds have been calculated. These polarizations are denoted by s_X, s_Y, p_X, and p_Y as defined in Fig. 1. The single-domain spectra have been analyzed with respect to the contributions from different initial states (specific bulk bands or surface resonances). This is illustrated in Figs. 5 and 6. As pointed out in Sec. II C, only IS of particular symmetries contribute to the single-domain spectra. The final 2PPE spectra for two-domain Si(001) surfaces (in Figs. 2 and 3) have been obtained by summing over all IS contributions and averaging over the orientations of the plane of incidence of light relative to the dimer rows. Accordingly, the capital letters in the spectra refer to the IS from which the contribution originates.[118]

The binding energies ε_i of the IS are related to the positions E_{kin} of the peak maxima by energy conservation, $\varepsilon_i = E_{\mathrm{kin}} + \xi - 2\hbar\omega$, where ξ denotes the ionization energy.[119] The dependence of the binding energies on photon energy (the peak dispersions) is displayed in Fig. 7. In contrast to surface-state peaks that reside at an essentially fixed IS energy, peaks derived from bulk states usually disperse with photon energy. This is due to the dispersion of the band energy of the IS with Bloch momentum $\mathbf{k}_\perp$ perpendicular to the surface. A particular feature of 2PPE are peaks that show a dispersion of the kinetic energy with $\hbar\omega$, which indicates the presence of a nondispersing IMS at the energy $\varepsilon_m = E_{\mathrm{kin}} + \xi - \hbar\omega$. Such an IMS couples to varying IS with binding energies that disperse downward with a slope of -1. Peaks that meet this condition and some candidates for constant IMS are highlighted in Fig. 7.

The assignment of the spectral peaks to IS and to the associated transitions to IMS is shown in Figs. 8 and 9. The figures contain the occupied and unoccupied parts of the bulk band structure and surface resonances at the $\mathbf{k}_\parallel$ points relevant for normal emission. Bulk states, i.e., the valence and conduction band states, have been identified with occupied and unoccupied states from the slab calculation in the way described in Ref. 100. The surface features are discussed in Appendix A.

In the following two subsections we discuss the origin and photon energy dependence of the individual peaks observed in the calculated spectra and compare to the experimental peaks and assignments. The identification of IMS will be addressed in Sec. IV.

B. Discussion of the theoretical spectra (initial states)

The following discussion is based on the decomposition of the single-domain spectra into IS contributions in Figs. 5 and 6.

(1) The prevailing feature in the s-polarized spectra is the broad (double) peak S-S' which is due to emission from the dangling-bond resonances D_{up}, D'_{up}, and the $\Delta_{2'}$ bulk band (see Fig. 8). For most $\hbar\omega$, the structure is preferably fitted by a double-peak ansatz. The intensity increases up to $\hbar\omega \approx$ 4.20–4.35 eV. Above this point, the peak as a whole disperses downward. In p-polarized light, the peak resides at higher kinetic energies, the intensity maximum is reached somewhat later, and the downward dispersion of S' sets in later. In contrast to s-polarized light, the upper component S disperses upward again above $\hbar\omega = 4.5$ eV.

(2) The additional main peak component B in p-polarized light has its origin in the upper parts of the Δ_5 band (see Fig. 8). It resides at about the same kinetic energies as S. The intensity of B is comparable to S-S' and the trends with photon energy observed for S-S' hold similarly for B. This seems plausible since, in the vicinity of Γ, the IS bands Δ_5 and $\Delta_{2'}$ are close in energy and the same unoccupied bands are involved in the emission process for both peaks (see Sec. IV B).

(3) Peak K occurs only in p_Y-polarized light. It is due to emission from the nearly flat "$-$" band of B_2 symmetry along Σ-L (Fig. 8), and accordingly, it shows only little dispersion. The intensity assumes a broad maximum at $\hbar\omega \approx 4.4$ eV. Peak K is the only peak that is clearly visible beside the main peak. All other structures in the theoretical spectra have to be magnified in order to be of comparable intensity.

(4) The structure I-I' is excited only in s_X- but not in s_Y-polarized light. It arises from the flat A_1-symmetric band along Σ'-L' at binding energies $\varepsilon_i \approx -1.2$ eV (see Fig. 9). The intensity steadily increases with photon energy. In p_X-polarized light, it reduces to one fourth as is expected if no additional IMS become available. Altogether, there are four degenerate flat bands along Σ-L and Σ'-L', two of which give rise to spectral features (K and I).

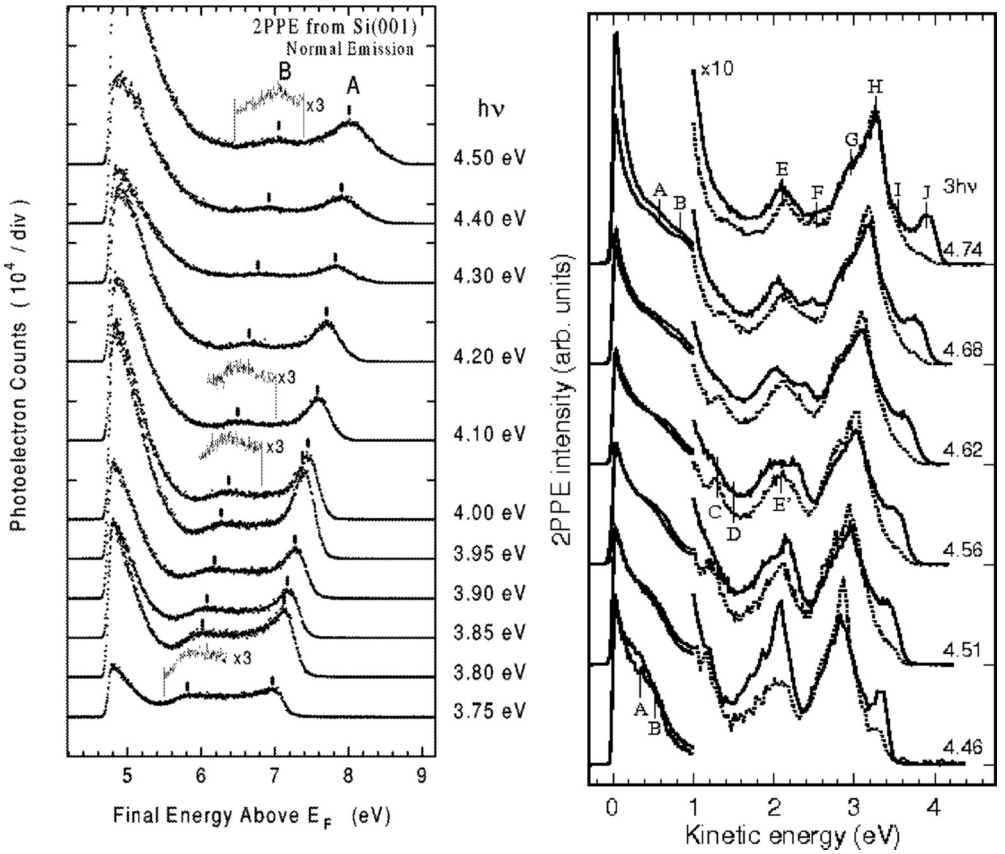

FIG. 4. Experimental 2PPE normal-emission spectra for a two-domain Si(001) surface. Left panel: Spectra by Shudo and Munakata, reproduced from Fig. 1 of Ref. 89. Right panel: Spectra by Kentsch *et al.*, reproduced from Fig. 3 of Ref. 90. The photoemission geometry is the same as in the calculated spectra. For the spectra in the left panel, p-polarized light has been used; the spectra in the right panel are for s- and p-polarized light (dashed and solid lines, respectively). When comparing to experiment, one has to keep in mind that the background of inelastically scattered electrons is absent in the theoretical spectra.

(5) Contrary to I, the structure J is present mainly in s_Y- but virtually not in s_X-polarized light. At $\hbar\omega \approx 4.35$ eV, the substructures D and H appear. J can be ascribed to the top region of the "+" band of A_1 symmetry along Σ-L (Fig. 8), while D and H issue from the dispersing part of this band. The emission from the corresponding "+" band of B_1 symmetry is negligible in contrast. The peak positions are approximately fixed at binding energies $\varepsilon_i \approx -1.35, -1.7,$ and -2.55 eV, respectively. The intensity shows a moderate increase with $\hbar\omega$. In p-polarized light, J appears for all photon energies with maximum intensity at $\hbar\omega \approx 4.35$ eV.

(6) The feature E in p-polarized light originates from the dispersing parts of Δ_5 (see Fig. 8). The emission becomes appreciable only at the highest $\hbar\omega$ where E exhibits a downward dispersion with a slope of ≈ -1 (as would be characteristic for a constant IMS; see Fig. 7).

(7) Finally, M enters the s-polarized spectrum at $\hbar\omega \approx 4.25$ eV as the only noticeable emission from below $\varepsilon_i = -3$ eV. The intensity is stronger in s_X- than in s_Y-polarized light and it doubles in p-polarized light. M arises from the $2\times$ backfolded bulk band of A_1 symmetry (right panel of Fig. 9). The structure M' in p-polarized light is due to the corresponding occupied bands of symmetries B_1 and B_2. The same conduction bands as for M take part in the emission process for M'; only the electrical field components (in or normal to the surface plane) exchange their roles.

C. Comparison to experiment

In the *lower range of photon energies* we assign the two main features in the spectra of Shudo and Munakata,[89] denoted by A and B (see Fig. 4), to the two broad peaks of the computed p-polarized spectra, decomposed into S-S'-B and K-I-J, respectively. In agreement with theory, the experimental structure B is mainly present in p-polarized light (see Ref. 89). The resonance of A found in experiment at $\hbar\omega = 3.95$ eV has been interpreted by Schattke *et al.* in Ref. 87 as a double resonant vertical bulk band transition occurring at a certain value of the Bloch momentum $k_\perp$. It has been remarked by the authors that the resonance energy can be brought into agreement with experiment if the band gap correction is adjusted to 0.3 eV (the value of $k_\perp$ shifts with varying band gap). As we apply a scissor operator of 0.6 eV, the exact matching conditions $(\hbar\omega)_{\rm res} := \varepsilon_f(k_\perp) - \varepsilon_m(k_\perp) = \varepsilon_m(k_\perp) - \varepsilon_i(k_\perp)$ for the bulk band transitions $\Delta_{2'}, \Delta_5 \to \Delta_5 \to \Delta_{2'}$ occur at $(\hbar\omega)_{\rm res} = 4.1$–$4.2$ eV. Moreover, in order to resolve the narrow resonance, a lower value of the optical potential

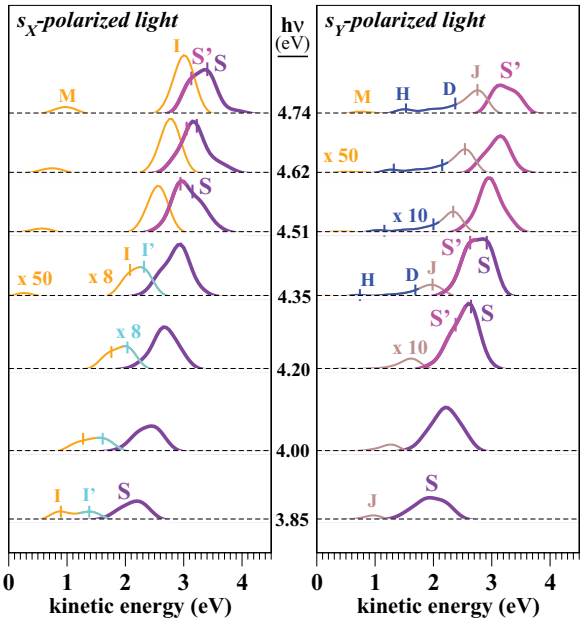

FIG. 5. (Color online) Polarization analysis and decomposition into IS contributions for the s-polarized 2PPE spectra. The electric field vector lies in the surface plane and is either perpendicular (left panel, s_X polarization) or parallel (right panel, s_Y polarization) to the direction of the dimer rows. The individual contributions have been scaled up by different factors that are specified at the graphs. For each contribution, the same magnification has been applied for all $\hbar\omega$, so that one readily obtains an overview of the photon energy dependence of the intensity for each single peak. The colors in the online version of this paper correspond to the ones used in Fig. 2.

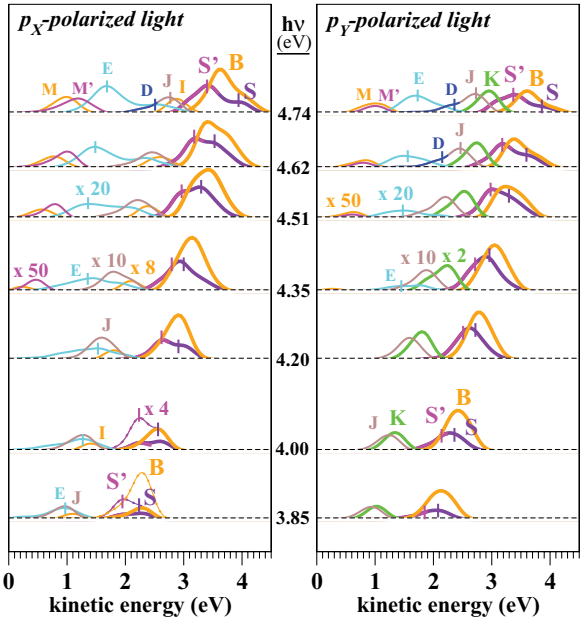

FIG. 6. (Color online) Same as Fig. 5 but for the p-polarized 2PPE spectra. Magnification factors are applied as explained in Fig. 5. An additional scaling has been applied to the structures S-S' and B for the lowest $\hbar\omega$ in p_X-polarized light to obtain the thin curves. The colors correspond to Fig. 3.

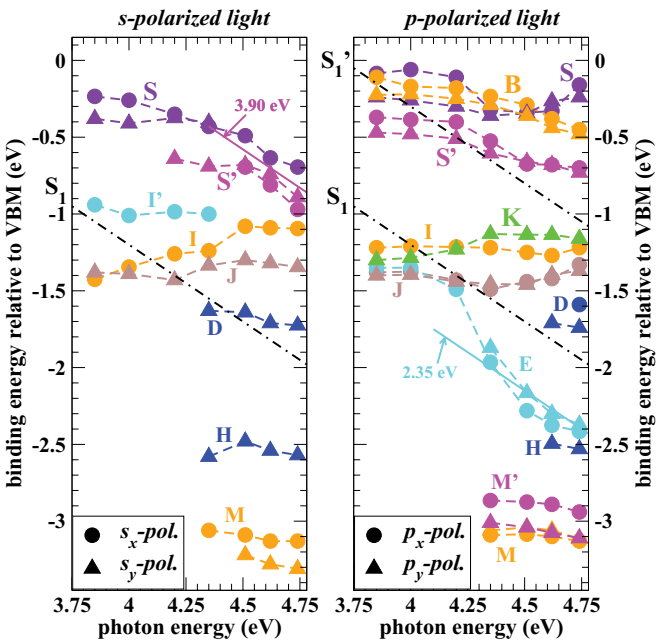

FIG. 7. (Color online) Photon energy dependence of the structures identified in the theoretical 2PPE spectra for s- and p-polarized light (left and right panel, respectively). Peak positions in the s_X- and p_X-polarized spectra are symbolized by circles, whereas triangles identify peaks in the s_Y- and p_Y-polarized spectra. The colors correspond to Figs. 2, 3, 5, and 6. The solid straight lines with a slope of -1 characterize peak dispersions that would fit an IMS, i.e., would be consistent with transitions via a constant IMS at the specified energy. The dash-dotted lines represent the positions of surface resonances (S_1, S_1') that could be of importance in the emission process; see Sec. IV and Appendix A.

acting on the IMS as the one applied here [$\mathrm{Im}(v_{\mathrm{opt}}) \approx 0.5$ eV] would be required. Accordingly, in p-polarized light, we observe only a very broad maximum at higher photon energies around $\hbar\omega \approx 4.35$ eV (Fig. 3); see the description in Sec. IV B.

The following refers to the *upper range of photon energies* above $\hbar\omega = 4.5$ eV and the spectra of Kentsch *et al.*[90] Table III gives an overview of the experimental and theoretical peak data.

The most intense peak aggregation in the spectra of Kentsch *et al.*[90] that comprises the peaks G, H, I, and J (the continuation of A of Ref. 89; see Fig. 4) falls into the same energy range as the theoretical peak complex that consists of the peaks S, S', and B in s- or p-polarized light. Since, after convolution, the resolution of the calculated spectra is less fine than in experiment, the fine structure of the experimental peaks cannot be reproduced well. Based on the s-polarized spectra, we identify our peak S' with the experimental peak H. A similar downward dispersion of the IS energies along $\Delta_{2'}$ with $\hbar\omega$ as in experiment is observed.

The main *polarization effect* in the spectra of Kentsch *et al.* seems to be the appearance of peaks I and J in p-polarized light. Energetically, these peaks correspond approximately to peak B and to the position of S in p-polarized light. Also the assignment to IS bands proposed by Kentsch *et al.* agrees with our ascription. The relative contribution of Δ_5 to the p-polarized spectra is more pronounced in theory (peak B)

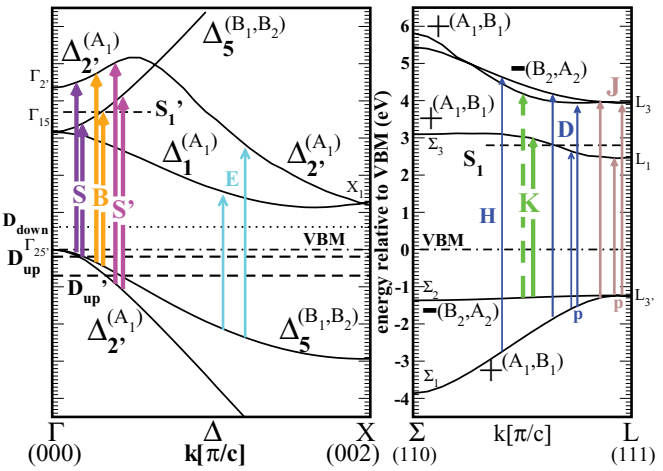

FIG. 8. (Color online) Initial and intermediate states of 2PPE. Bulk band structure of Si along the Δ line (left panel) and along the Σ-L line in reciprocal space (right panel) that is folded back to the Δ line for the (2 × 1)-reconstructed surface. The signs ("+" and "−") refer to the parity of the states with respect to the mirror symmetry σ_v. This designation of the bulk bands follows the one in Ref. 90. C_{2v}-symmetric states (transforming according to representations A_1, etc., as denoted) are superpositions of energetically degenerate Bloch states with wave vectors from the star created by application of C_{2v} point group operations to **k**. The LDA Kohn-Sham eigenenergies in the unoccupied part are shifted upward by a band gap correction of $\Delta\varepsilon \approx 0.6$ eV. In addition to the bulk bands, several surface resonances in the range of occupied and unoccupied states are marked by horizontal lines. The identified transitions are indicated by arrows; the colors (in the online version of this paper) correspond to Figs. 2, 3, and 5–7. Dashed arrows denote transitions that are of minor importance in the origin of a given peak.

than in experiment (peak I) but it may be that part of the emission from Δ_5 contributes to H in experiment. The role of the IMS in the polarization effect is discussed in Sec. IV B.

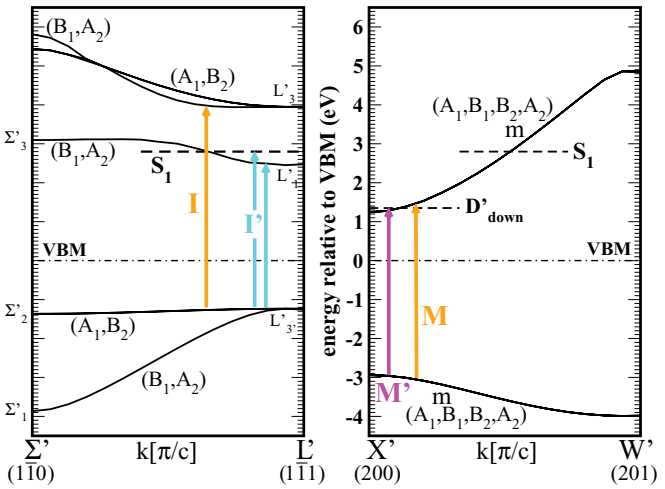

FIG. 9. (Color online) Initial and intermediate states of 2PPE (continued). Bulk band structure of Si along the two additional lines in reciprocal space that are folded back to the Δ line in case of the full $p(2 \times 2)$ reconstruction. For the creation of C_{2v}-symmetric states and for the transitions, see Fig. 8.

TABLE III. Comparison of the peaks in the experimental spectra by Kentsch *et al.* (Ref. 90) (left part) to the structures in the calculated spectra (right part) for photon energies $\hbar\omega \geqslant 4.5$ eV. The binding energies ε_i refer to $\hbar\omega = 4.62$ eV. For theoretical peaks that are present in both s- and p-polarized light ($s + p$), the values refer to the p-polarized spectra. The assignment to IS is given in addition ("+" and "−" denote bulk bands according to Fig. 8). The values $\bar{\alpha}$ denote the approximate slope of the kinetic energies of the peak positions in the experimental spectra with respect to photon energy $\hbar\omega$. Values that refer to the experimental spectra are taken from Tables III and IV in Ref. 90.

Peak	Pol.	ε_i (eV)	IS	$\bar{\alpha}$	Peak	Pol.	ε_i (eV)	IS
J	p	−0.20	D_{up}	2.0	S	p	−0.31	D_{up}
I	p	−0.48	Δ_5	1.8	B	p	−0.40	Δ_5
H	$s + p$	−0.74	$\Delta_{2'}$	1.4	S'	$s + p$	−0.68	$\Delta_{2'}$
G	$s + p$	−1.01		1.1	I	$s(p)$	−1.09	$\Sigma' L'(A_1)$
F	p	−1.48	−	1.7	K	p	−1.14	$-(B_2)$
E'	s	−1.75		0.5	J	$s + p$	−1.41	$+(A_1)$
E	p	−1.84	+	1.1	D	$s + p$	−1.71	$+(A_1)$
D	s	−2.16		1.3				
C	s	−2.48		1.1	H	s	−2.50	$+(A_1)$
					E	p	−2.35	Δ_5
B	$s + p$	−3.14		1.1	M, M'	$s + p$	−2.95	"m"
A	$s + p$	−3.35		0.8			−3.08	

The low-energy shoulder G in the experimental spectra is not reproduced by our theory. Based on the slope $\bar{\alpha} \approx 1$ and the energetic position, the assignment of G to the local band minimum Γ_{15} has been suggested by Kentsch *et al.* This explanation, which assumes that G is due to an IMS populated indirectly by inelastic scattering, is compatible with the absence in the theoretical spectra.

The group of experimental peaks E, F, and E', i.e., the peak aggregate around 2 eV kinetic energy, should be compared to the structures I, K, and J-D in theory. It seems most likely that the peaks in this energy range (-2 eV $< \varepsilon_i <$ -1 eV) essentially originate from the backfolded bands along Σ-L (and the corresponding line Σ′-L'; see Figs. 8 and 9). Generally, the intensity of this group relative to the main peak complex is distinctly larger in the spectra by Kentsch *et al.* than in theory. An exception is the theoretical peak K. We therefore start by assuming the correspondence of K to the experimental peak F. Although F appears lower in energy than K by 300–350 meV, the position at the high-energy end of the peak aggregation, the polarization dependence, and a slope not far from $\bar{\alpha} = 2$ make the assignment likely.

For the structure I in theory we have not found any corresponding peak in the experimental spectra. This may be due to the particular $p(2 \times 2)$ reconstruction that is required for I. Other possible explanations are that I is either part of the low-energy side of the main peak complex or that I is lower in energy similar to the shift proposed for K, i.e., at about the same position as F, and in the high-energy side of the experimental peak E'. An overall shift of 350 meV would bring the position of the theoretical group of peaks (K, I, and J-D) into better agreement with experiment.

It is likely that the experimental peak E in p-polarized light is related to the theoretical peaks J and D. The assignment of E

by Kentsch *et al.* to the IS "+" band agrees with our assignment of J and D. E' could correspond to J-D in s-polarized light where it rests on nonresonant transitions via a virtual IMS; see the discussion in Appendix B. Another aspect is that there is evidence[99] for a more prominent role of the surface resonance denoted by S_1; see Appendix A. It is possible that the direct or indirect excitation of S_1 is actually stronger than in our calculations which could enhance the theoretical peaks in both s- and p-polarized light.

Peaks C and D in the experimental spectra occur only in s-polarized light but D is hardly visible for $\hbar\omega \leqslant 4.75$ eV.[90] In view of the polarization dependence, it is possible that C may be assigned to H in theory.

The structure E in the calculated spectra, which originates from Δ_5, resides at kinetic energies where no peaks are observed in the experimental p-polarized spectra. Only via relaxation toward the conduction band minimum could it come closer to the experimental peak B. The small peaks A and B in experiment appear in the same energy range of binding energies below $\varepsilon_i = 3$ eV as the faint structures M and M' in theory that require a (2×2)-reconstructed surface. The experimentally observed slopes of $\bar{\alpha} \approx 1$ suggest that here also an indirectly excited IMS is involved. This could be the D'_{down} resonance (see Fig. 9).

The experimental intensities for some of the weaker structures are stronger than in theory if the above assignments are taken as a basis. Scattering experienced in the excited state is likely to affect the peak positions and intensities. Due to the optical potential, a considerable part of the excitation is lost in the calculation. The strong scattering is confirmed by the considerable background of secondary electrons in the experimental spectra. The *indirect excitation of IMS*, that is, population via scattering, could be of importance,[114] which is supported by the fact that several of the experimental peaks show dispersions close to $\bar{\alpha} \approx 1$ that are not likely to result from IS dispersions. Another uncertainty concerns the *screening of the external field* that is not accounted for in the calculated spectra. Local field effects may lead to considerable changes in the photoemission intensities. Altogether, this indicates that a complete description of 2PPE spectra will require a more realistic inclusion of many-particle effects during excitation.

IV. INTERMEDIATE STATES

A. General considerations

In the present section, the spectra will be analyzed with regard to the IMS that are involved in the photoemission process. The analysis is based on the perturbation expansion[120] Eq. (4). The wave functions of the *intermediate states* with energies below the vacuum threshold are obtained as bound Kohn-Sham eigenstates of the slab. They are unoccupied in the ground state. The LDA eigenenergies are modified according to $\varepsilon_m^{\text{LDA}} \rightarrow \varepsilon_m^{\text{LDA}} + \Delta\varepsilon$ to account for the band gap correction $\Delta\varepsilon$. Furthermore, a finite imaginary part of the self-energy, $-i\eta_m$, is assumed.

The *final states* are eigenstates of $\hat{H}_0$ that represent scattering states at a given kinetic energy with proper asymptotic behavior, i.e., time-reversed LEED states. Simulations of a LEED-type electron scattering experiment in the time domain have been performed, in which the time evolution of a Gaussian wave packet is calculated that is initially incident along the surface normal. These simulations employ absorbing boundary conditions as in the photoemission simulations. The wave packet is initially localized between the crystal surface and the absorbing layer. Its center is located at a separation of $35a_0$ from the crystal surface and of $15a_0$ from the onset of the absorbing potential. Its width amounts to $4a_0$. The wave number is centered around $k_0 = 0.38$–0.61 a.u. corresponding to a kinetic energy of $k_0^2/2 = 2.0$–5.0 eV. The wave packet impinges onto the surface, where it is scattered. Part of the wave packet is reflected into the different directions determined by the reciprocal lattice of the surface. The other part is absorbed by the optical potential in the bulk which accounts for inelastic scattering within the crystal. Finally, also the reflected part is absorbed at the boundary, and the wave function becomes approximately zero again within the supercell after some femtoseconds. By Fourier transform to the frequency domain, one obtains wave functions that, within a subcell region, coincide with scattering eigenstates of the slab. The subcell is sufficiently large to contain the region where the wave functions of the bound states (IMS) essentially differ from zero. Hence the matrix elements between the IMS and the FS (as constructed from the LEED states) can be calculated.

According to Eq. (4), the 2PPE photocurrent from a fixed IS $|i\rangle$ in general originates from the coherent superposition of contributions of different IMS. In the simplest case, there is only one IMS $|m\rangle$ that couples significantly to the IS under consideration, while the other matrix elements $M_{\text{mi}} = \langle m|\hat{O}|i\rangle$ are negligible. In this case the contribution from $|i\rangle$ simplifies to

$$\frac{R^2 j_{\mathbf{R}}(\varepsilon)}{v} \propto \left| \frac{\langle f(\varepsilon)|\hat{O}|m\rangle\langle m|\hat{O}|i\rangle}{\varepsilon_i - \varepsilon_m + \omega + i\eta_m} \right|^2, \quad \text{with} \quad \varepsilon = \varepsilon_i + 2\omega. \tag{6}$$

Note that quasielastic scattering events—due to the coupling to phonons, scattering via defects, or the decay of the created photohole, etc.—that are frequently described phenomenologically by a so-called "pure dephasing" rate in the initial and intermediate state are not included here. Our Eq. (6) corresponds to Eq. (A11) in the paper by Wolf *et al.*[114] and to Eq. (14) in Ueba and Gumhalter[83] in the limit of vanishing pure dephasing in the final state (i.e., $\Gamma_f^* = 0$ beside $\Gamma_i^* = \Gamma_m^* = 0$).

If the matrix element $M_{\text{fm}}(\omega) = \langle f(\varepsilon_i + 2\omega)|\hat{O}|m\rangle$ that describes the coupling of the IMS to the FS is assumed to be independent of the energy of the FS, then Eq. (6) yields a Lorentzian curve for the photon energy dependence of the photoemission intensity from the single fixed IS $|i\rangle$. This is shown schematically in Fig. 10. The energy ε_m and optical potential (i.e., the imaginary part of the self-energy) η_m in the IMS determine the position and width of the resonance.

However, the significance of final-state effects is well known from the theory of 1PPE; see, e.g., Ref. 117. In the context of 2PPE, this enters as "1PPE from the IMS," where the FS and therewith the matrix element $M_{\text{fm}}(\omega)$ for the second transition will in general show some variation with photon energy. If, in first order, a linear dependence

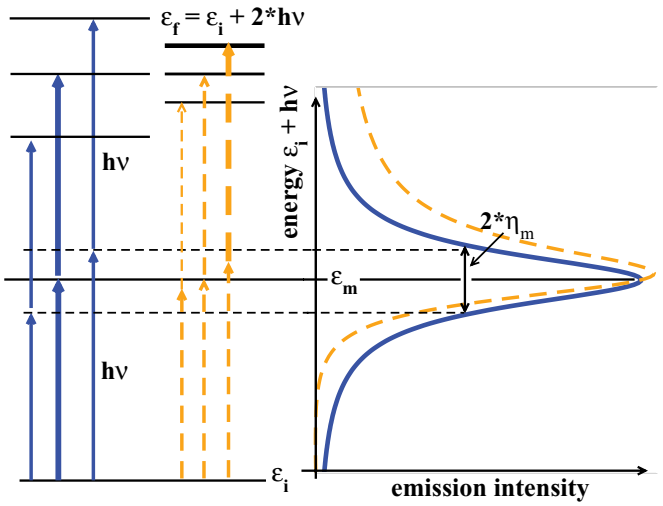

FIG. 10. (Color online) Resonance curve Eq. (6). The solid (blue) curve in the right panel shows the emission intensity [here defined as the left-hand side of Eq. (6)] from a constant IS (with energy ε_i) if there is only one IMS available (with energy ε_m), and if the matrix elements with the FS (with energies ε_f) are approximately constant. The associated energies and transitions around the resonance condition $\hbar\omega = \varepsilon_m - \varepsilon_i$ for the first transition are indicated in the energy diagram to the left. The energy and inverse inelastic lifetime of the IMS, ε_m and $2\eta_m$, can be read off from the position and width of the intensity distribution. An ω-dependent matrix element $M_{\rm fm}(\omega)$ can distort the resonance curve as indicated by the dashed (orange) line.

$M_{\rm fm}(\omega) = \alpha\omega + \beta$ (with complex numbers α and β) is assumed, the resonance curve of Fig. 10 is modified in a way indicated by the dashed curve, that is, alongside with a slight asymmetry, this final-state effect should mainly lead to a *shift of the resonance position*. This will further be illustrated in Sec. IV B on the basis of the calculated Si(001) 2PPE spectra.

What can be said about the assumption of a single relevant IMS that leads to the considerable simplification in Eq. (6)? As has been pointed out by Schattke *et al.*,[87] if the transition from the IS to the IMS takes place in the bulk, it obeys a selection rule with respect to the Bloch momentum $\mathbf{k}_\perp$ perpendicular to the surface; that is, it corresponds to a vertical transition in the bulk band structure. Based on this assumption and using the known occupied band structure, mapping of an unoccupied copper bulk band by angle-resolved 2PPE has been reported recently.[88] In the optimum case, spectroscopy of a constant IS at $\mathbf{k}$ may reveal the unoccupied states at $\mathbf{k}$ as successive resonances in 2PPE if they are sufficiently separated with respect to their energy. This is facilitated by adjusting the polarization of the light so as to keep the symmetry selection rules as restrictive as possible. Otherwise, IMS of different symmetries but close in energy may interfere.

Furthermore, bulk states at the same energy but with different $\mathbf{k}_\perp$ may be scattered into one another at the surface, where $\mathbf{k}_\perp$ is not sharply defined any longer. For reconstructed surfaces, the hybridization of energetically degenerate states with $\mathbf{k}_\parallel$ that differ by reciprocal lattice vectors of the surface further complicates the situation. Surface resonances—occupied as well as unoccupied—tend to be dipole coupled to different states relatively close in energy. Thus, the presence of the surface in general furthers interference of excitation paths via different IMS which corresponds to the more complicated expression of Eq. (4) with several IMS retained.[121] On the other hand, an "irregular" behavior observed in 2PPE spectra due to such interference effects may give a hint of the presence of a surface-induced feature. This is illustrated by the recent description of a Fano-type resonance by Eickhoff *et al.*[98] in 2PPE spectra from Si(001) that occurs between the $D_{\rm up}$ state and the lowest IPS where both states hybridize with the continuum of bulk bands.

B. Role of intermediate states in the origin of the main peaks of the Si(001) 2PPE spectra

In this section the role of the unoccupied states as IMS in the origin of the main peaks S-S', B, and K (see Sec. III B) is investigated. This is done in the light of the general considerations of the preceding subsection. The less intense structures are discussed in Appendix B. The energies ε_i and ε_m of the IS and IMS associated with the identified transitions are compiled in Table V and the energy differences $\Delta\varepsilon = \varepsilon_m - \varepsilon_i$ are compared to the positions $(\hbar\omega)_{\rm max}$ of maximum intensity.

(1) In s-polarized light the IMS for S-S' are states from the Δ_5 conduction band. For each of the single discrete IS belonging to $\Delta_{2'}$,[122] one single vertical transition to the IMS selected from Δ_5 by conservation of $\mathbf{k}_\perp$ prevails, and the single-state emission intensity curves have the resonance shape of Fig. 10. Accordingly, S-S' should be considered as a peak that essentially rests on the *bulk transition* $\Delta_{2'} \rightarrow \Delta_5$. This is in agreement with the observed insensitivity of this peak to oxygen adsorption in Ref. 90 and to the assignment in Ref. 87. According to the $\mathbf{k}_\perp$ dispersion of the two bands in the transition $\Delta_{2'} \rightarrow \Delta_5$, the single-state curves pass through resonance at successive $(\hbar\omega)_{\rm max}$. However, there is a FS effect of the type displayed in Fig. 10 that produces an upward shift of all resonance positions so that the onset of significant emission occurs at higher $\hbar\omega$ than is expected from the minimum band distance of $(\Delta\varepsilon)_{\rm min} \approx 3.25$ eV at Γ. Furthermore, instead of reflecting the true dispersion of the IMS band Δ_5, the peak dispersion takes the appearance of a constant IMS at $\varepsilon_m \approx 3.9$ eV (straight line in Fig. 7). This example shows that some care has to be taken when deriving energies of IMS from peak dispersions in 2PPE spectra; see the remarks in Ref. 123 on this point.

In p-polarized light at higher $\hbar\omega$, the unoccupied $\Delta_{2'}$ band becomes available as an additional IMS band whereby the matrix elements are of comparable magnitude. We note that in the absence of any modifying FS effect, one should observe two successive resonances for each IS in p-polarized light according to the transitions $\Delta_{2'} \rightarrow \Delta_5$ and $\Delta_{2'} \rightarrow \Delta_{2'}$. Due to the upward shift of the lower resonance and the relatively broad width of the resonances, there is a range of $\hbar\omega$ in which the two contributions overlap. For the lower part of $\Delta_{2'}$ (peak S') the two resonances are not resolvable in the computed spectra, and only the intensity maximum is slightly shifted toward higher $\hbar\omega$ in p-polarized light. In contrast, for $D_{\rm up}$ and the upmost part of $\Delta_{2'}$, the upper resonance is observed separately from the lower one, which is reflected in the final upward dispersion of peak S in p-polarized light.

(2) The same unoccupied bands, Δ_5 and $\Delta_{2'}$, serve as IMS for the Δ_5 valence band, i.e., the peak component B in the p-polarized spectra. Since the matrix elements are roughly of the same magnitude, the overall appearances of B and S-S' are rather similar. However, B resides at slightly higher kinetic energies, which accounts for the major part of the observed polarization effect. Corresponding to S, i.e., to D_{up}, there is a tendency in B to form a high-energy shoulder according to the transition $\Delta_5 \rightarrow \Delta_{2'}$ for $\hbar\omega \geqslant 4.5$ eV. This can be seen in Fig. 6. The transition $\Delta_5 \rightarrow \Delta_1$ plays only a minor role. It is expected to be resonant below $\hbar\omega = 3.85$ eV, and there it should become more prominent.

(3) The main excitation path for peak K involves the unoccupied "+" (A_1) bands. The lower of the two "+" conduction bands couples stronger and is energetically favorable. In particular, IMS at $\varepsilon_m \approx 3.3$ eV that are likely to represent the upper band edge prevail in the emission process. The maximum intensity of K at $(\hbar\omega)_{\mathrm{max}} \approx 4.2$–$4.5$ eV corresponds to an IMS energy of $\varepsilon_m \approx 3.1$–$3.4$ eV. Note that since the IS band is almost nondispersing, the IMS manifest themselves only in form of a broad resonance in the $\hbar\omega$-dependent intensity but do not appear as a characteristic dispersion over a wider range of $\hbar\omega$.

V. SUMMARY AND OUTLOOK

A series of normal emission 2PPE spectra for the Si(001)$p(2 \times 2)$ surface has been calculated by direct simulation of the photoemission currents excited by a fs-laser pulse. As the time-dependent wave functions inherently contain the contributions to the photocurrent to, in principle, arbitrary order, 2PPE spectra can easily be derived from the simulations. In the present work, the effective potential has been kept frozen to its ground-state value obtained within DFT-LDA. Inelastic electron scattering events are only considered as a loss mechanism in the intermediate and final states. The losses are approximately accounted for by an optical potential.

The assignment of photoemission peaks to valence bands is based on the decomposition of the spectra into initial-state contributions at given polarization of the light and orientations of the surface domains. An overall good agreement with the experimental peak dispersions is obtained. In order to analyze the excitation paths, i.e., to determine the intermediate states involved in the 2PPE process, the dipole matrix elements with both initial and final states have been evaluated. This allows us to identify bulk transitions in the Si(001) spectra along the lines of the general considerations in Ref. 87. The analysis further shows that, in several instances, quantum mechanical interference between different excitation paths and, moreover, final-state effects have to be taken into account.

The deviations of the relative 2PPE peak intensities in theory and experiment may partially be due to approximations in the theory, e.g., the neglect of screening of the laser field and the rough description of inelastic lifetimes by a constant (state-independent) optical potential. The detailed comparison of theoretical and experimental peaks further suggests that indirect excitation of unoccupied states that become populated via inelastic scattering may play a role. It would be feasible to determine the screening response in a separate self-consistent TDLDA calculation with the optical potential set to zero. The screened excitation field can then be plugged into a subsequent 2PPE calculation. This procedure is, however, beyond the scope of the present paper.

The time-dependent simulation approach goes beyond the well-known expressions from the perturbation expansion for 2PPE in that it opens the opportunity for novel future research, in particular the investigation of correlation effects on very short time scales in time-dependent experiments.

ACKNOWLEDGMENTS

Financial support by the Innovationsfond des Landes Schleswig-Holstein is gratefully acknowledged. The numerical computations have been carried through at the Rechenzentrum der Universität Kiel.

APPENDIX A: Si(001) SURFACE-PROJECTED DENSITY OF STATES

In this Appendix we investigate the surface electronic density of states of the Si(001)$p(2 \times 2)$ in the energy range of the IMS. Figure 11 shows the surface projected density of states (surface PDOS) that has been derived from the Kohn-Sham band structure solely at $\bar{\Gamma}$. The eigenenergies have been shifted by the band gap correction of 0.6 eV. As opposed to the dangling-bond states D_{down} and D'_{down}, the surface-enhanced PDOS features S_1, S'_1, and S''_1 do not give rise to pronounced surface states or resonances in the PDOS but rather correspond to moderate surface enhancements. They are

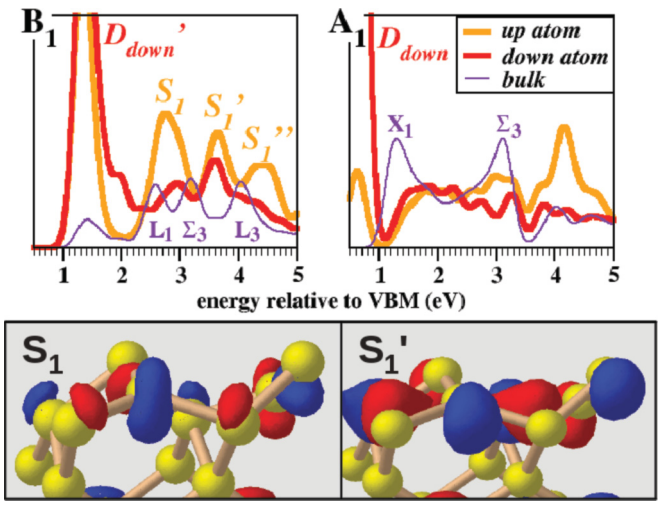

FIG. 11. (Color online) Upper panel: Surface-projected density of states at the $\bar{\Gamma}$ point for the Si(001)$p(2 \times 2)$ surface. Electronic structure calculated for a slab with 36 layers. The curves correspond to a sum over the projections of the symmetry-selected Kohn-Sham wave functions onto the $3s$ and $3p$ orbitals of the $\mathrm{Si}_{\mathrm{up}}$ and $\mathrm{Si}_{\mathrm{down}}$ dimer atoms convoluted with a Gaussian of 140 meV width. For comparison, the bulk DOS is shown. Left (right) panel: B_1- (A_1-) symmetric states. The positions of the surface enhancements are indicated. Table IV lists the approximate energetic positions and the bulk bands with which hybridization occurs. Lower panel: Contour surfaces for surface-enhanced eigenstates belonging to S_1 and S'_1. The colors in the online version (red and blue) denote opposite phases of the wave function.

TABLE IV. Approximate energetic positions of the surface resonances shown in Fig. 11 and bulk bands with which hybridization occurs.

State	Symmetry	Energy ε_m (eV)	Related bulk bands
D_{down}	A_1	0.6	
D'_{down}	B_1	1.35	"m"
S_1	B_1	2.8	$+$, $\Sigma' L'$ & "m"
S'_1	B_1	3.65	Δ_5
S''_1	B_1	4.5	$+$, $\Sigma' L'$ & "m"

listed in Table IV. The orbital character in the topmost layers can be read from the contour plots in the lower panel of Fig. 11.

S_1, S'_1, and S''_1 are of positive parity with respect to the mirror plane containing the dimer atoms. A common feature is the *antibonding character of the back bonds* between dimer and second layer atoms. If both dimer atoms have nonvanishing contributions to the wave function, then only in case of the B_1-symmetric states, where the wave function changes sign under the C_2 symmetry operation, is an antibonding character with respect to the dimer atoms obtained. Based on the similarity of the wave functions, we speculate that S_1, S'_1, and S''_1 may be part of a very broad resonance with hybridization to several bulk bands.

We further suggest that S_1, centered at around $\varepsilon_m \approx 2.8$ eV, may be related to the resonance in 2PPE from the D_{up} state at photon energies around $\hbar\omega \approx 3$ eV reported by Fauster *et al.*[99] Based on the energetic position of the resonance and a polarization analysis of the spectra, Fauster *et al.* have assigned this resonance to an *antibonding dimer-bond state*, which had been predicted by Pollmann *et al.* in electronic structure calculations for a Si(001)(2×1) with buckled dimers using a half-space geometry.[124] From the energetic position of the resonance, this state was located at $\varepsilon_m \approx 2.83$ eV above VBM in Ref. 99.

The resonance energy of $\Delta\varepsilon \approx 3.75$ eV for the transition $D_{\text{up}} \rightarrow S'_1$ would approximately match with the position of the smaller resonance at $\hbar\omega \approx 3.8$ eV in the spectra of Shudo and Munakata in Ref. 89 (see Fig. 4). It may be that this transition is visible in addition to the strong bulk band transition (see Ref. 87 and Sec. IV B).

For completeness we note that there is also an enhancement in the case of the A_1-symmetric wave function around $\varepsilon = 4.2$ eV which, however, will not be considered further in view of its small weight. Moreover, unoccupied states with A_2 symmetry are not considered here since they do not contribute to normal emission 2PPE according to the selection rules (Table II).

APPENDIX B: INTERMEDIATE STATES IN THE Si(001) 2PPE SPECTRA (CONTINUED)

In this Appendix, the IMS that are relevant for the structures in the theoretical spectra with intensities clearly smaller than in the main peaks are discussed. We note that for most of these structures, the comparatively weak intensity is mainly owed to smaller matrix elements M_{fm} for the second transition to the FS whereas the first transition from the IS can be of a magnitude comparable to the main peak transitions. Thus, it is a FS effect that suppresses the signal from conduction band states that are strongly excited in the 2PPE process.

The following discussion is based on the spectra of Figs. 5 and 6; the numbers (4)–(7) refer to the enumeration of the peaks in Sec. III B.

(4) For peak I-I' in the s_X- (and p_X-) polarized spectra, the IMS belong to the two conduction bands of B_1 symmetry along Σ'-L' and to the surface resonance S_1, whereas the dipole coupling of the IS (A_1) band to either of the degenerate bands of symmetries A_1 and B_2 is negligible. The steady rise of intensity with $\hbar\omega$ for I (see Fig. 5) is consistent with the upper band as IMS, and the analysis indicates that the main contribution comes from the band bottom at $\varepsilon_m \approx 3.8$ eV. The extra peak I' is mainly due to a transition to S_1 and to the lower band in the vicinity of the L point (see Fig. 9). More generally spoken, the occurrence of a double peak at the lower $\hbar\omega$ reflects the existence of the two conduction bands. The maximum intensity for the transition to the lower band including S_1 is assumed below $\hbar\omega = 3.85$ eV.

(5) The different transitions identified for J, D, and H are displayed in Fig. 8, with the transitions that occur only in p-polarized light grouped to the right. In s-polarized light, only the transition $+ \rightarrow -$ is of importance. Similar to peak I, the energy difference $\Delta\varepsilon_{\text{min}}$ of more than 5 eV between the two bands accounts for the steady increase of emission with $\hbar\omega$ in s_Y-polarized light. The identified IMS from the "$-$" band for D and H are located at $\varepsilon_m \approx 4.15$ eV and 4.5 eV, respectively, so that one remains below the resonance condition for D and far below for H (see Table V). However, below resonance, one should expect that there is one peak that remains fixed at the $\mathbf{k}_\perp$ position that corresponds to the minimum energy distance $\Delta\varepsilon_{\text{min}}$ between the dispersing IS and IMS bands with a continuously increasing intensity when $\hbar\omega$ approaches $\Delta\varepsilon_{\text{min}}$ from below. This is just the interpretation of peak J. Only after the transition has first become resonant should the peak begin to disperse. A little different from this, in the present case, there seems to be an oscillatory emission from the "$+$" band as a function of $k_\perp$ with subpeaks at the nearly fixed positions of D and H and valleys in between. The analysis indicates that the simple picture in terms of one vertical bulk transition $+ \rightarrow -$ is complicated by the presence of the surface. Surface scattering leads to hybridizations between bulk states from the "$+$" and $\Delta_{2'}$ valence bands as well as from the "$-$" and Δ_5 conduction bands (see Fig. 8). Thus, the IS can be thought of as a coherent superposition of two different bulk band components. Accordingly, different IMS bands are excited coherently and the two bulk excitation pathways are brought to interference. For J, the contributions enter with nearly opposite phase, which results in a considerable weakening of the peak intensity. When $k_\perp$ is varied, the interference between the two bulk bands becomes alternately constructive or destructive.

In p-polarized light, the unoccupied "$+$" bands of A_1 symmetry, which are excited via the surface-normal field component, prevail as IMS in the emission process for J and D. As they tend to cancel the contributions from the unoccupied "$-$" band, the appearance of J-D is quite similar in p_X- and p_Y-polarized light. Both "$+$" bands yield contributions of comparable magnitude. The intensity maximum at $(\hbar\omega)_{\text{max}} \approx 4.6$ eV lies between the single resonance positions of the two

TABLE V. Transitions and associated energies for the features in the calculated 2PPE spectra. For each of the initial-state contributions (shown in Figs. 5 and 6), the table lists the identified transitions (Figs. 8 and 9), the energies of the corresponding initial and intermediate states, ε_i and ε_m, and the associated resonance energies, that is, the energy differences $\Delta\varepsilon = \varepsilon_m - \varepsilon_i$. This should be compared to the photon energies $\hbar\omega_{\max}$, at which the peaks reach maximum intensity. In the case of peaks that are present in both s- and p-polarized light, only the additional transitions that are excited by the surface-normal field component are listed in the row for p polarization. The specified IS energies belong to the respective photon energies $\hbar\omega_{\max}$.

Peak	Polarization of light	Transition $i \to m$	IS energy ε_i (eV)	IMS energy ε_m (eV)	Energy difference (eV)	Photon energy $\hbar\omega_{\max}$ (eV)
SS'	$\begin{cases} s_X, s_Y \\ p_X, p_Y \end{cases}$	$\Delta_{2'} \to \begin{cases} \Delta_5 \\ \Delta_{2'} \end{cases}$	$-0.6, -0.5$ -0.5	3.6,3.5 4.7	4.2,4.0 5.2	4.4,4.25 4.55,4.35
B	p_X, p_Y	$\Delta_5 \to \Delta_5$ & $\Delta_{2'}$	-0.25	3.5 & 4.6	3.75 & 4.85	4.3–4.4
K	p_Y	$-(B_2) \to +(A_1)$	-1.15	2.7–3.3	3.85–4.45	4.2–4.5
I	s_X	$\Sigma' L'(A_1) \to \Sigma' L'(B_1)$	-1.1	3.8–4.0	4.9–5.1	>4.75
I'	s_X	$\Sigma' L' \to \Sigma' L'$ & S_1	-1.0	2.5–2.8 & 2.8	3.5–3.8 & 3.8	<3.85
J	$\begin{cases} s_Y \\ p \end{cases}$	$+(A_1) \to \begin{cases} -(B_2) \\ +, +(A_1) \end{cases}$	-1.35 ≈ -1.4	≈ 4.0 2.5–2.8 & 4.0	5.35 3.9–4.2 & 5.4	>4.65 4.2–4.5
D	$\begin{cases} s_Y \\ p \end{cases}$	$+(A_1) \to \begin{cases} -(B_2) \\ +, +(A_1) \end{cases}$	-1.7 -1.7	≈ 4.15 2.6–2.8 & 4.0	5.85 4.3–4.5 & 5.7	>4.75
H	s_Y	$+(A_1) \to -(B_2)$	-2.5	4.5	7.0	>4.75
E	p	$\Delta_5 \to \Delta_1$ & $\Delta_{2'}$	< -2.4	1.4 & 2.7	>3.8 & 5.1	>4.75
M	s, p	$m(A_1) \to m$	< -3.15	1.65	>4.8	>4.75
M'	p	$m(B_1, B_2) \to m$	≈ -3.0	1.4	4.4	4.60–4.75

bands, so that, in contrast to I-I', the energetic separation of these two bands cannot be resolved in the theoretical spectra.

(6) The structure E arises from the transitions $\Delta_5 \to \Delta_1, \Delta_{2'}$. The dispersion of E in the upper range of photon energies would fit an IMS at $\varepsilon_m \approx 2.30$–$2.35$ eV (straight line in Fig. 7), whereby the intensity is still on the rise at $\hbar\omega = 4.75$ eV. Here, the evaluation of the matrix elements reveals that the IMS changes with increasing $\hbar\omega$ from Δ_1 to $\Delta_{2'}$. In this case, the constant IMS position from the dispersion of E only indicates the approximate position or energy range of the actual IMS.

(7) The emission process for M and M' is dominated by vertical transitions between the degenerate bulk bands (right panel of Fig. 9). This transition is of comparable strength for all three allowed symmetries, and only the stronger coupling to the FS in case of the A_1- and B_1-symmetric (as compared to the B_2-symmetric states) is responsible for the observed polarization effects. The photon energy at which M and M' appear just above the vacuum level coincides with the minimum band distance of $\Delta\varepsilon \approx 4.2$ eV, that is, with the onset of resonant emission between the dispersing bands. Most of the B_1-symmetric IMS exhibit a considerable surface enhancement related to the D'_{down} state. As this leaves their coupling to the IS bulk band rather unaffected, M and M' are nevertheless dominated by bulk transitions.

*husser@theo-physik.uni-kiel.de

[1] U. Bovensiepen, H. Petek, and M. Wolf (eds.), *Dynamics at Solid State Surfaces and Interfaces*, Vol. 1: Current Developments (Wiley-VCH, Weinheim, 2010).

[2] H. Petek and S. Ogawa, Prog. Surf. Sci. **56**, 239 (1997).

[3] H. Ueba and B. Gumhalter, Prog. Surf. Sci. **82**, 193 (2007).

[4] R. W. Schoenlein, W. Z. Lin, J. G. Fujimoto, and G. L. Eesley, Phys. Rev. Lett. **58**, 1680 (1987).

[5] J. Bokor, Science **246**, 1130 (1989).

[6] W. S. Fann, R. Storz, H. W. K. Tom, and J. Bokor, Phys. Rev. Lett. **68**, 2834 (1992).

[7] J. R. Goldman and J. A. Prybyla, Phys. Rev. Lett. **72**, 1364 (1994).

[8] R. Haight, Surf. Sci. Rep. **21**, 275 (1995).

[9] P. M. Echenique and J. B. Pendry, J. Phys. C **11**, 2065 (1978).

[10] P. M. Echenique, J. M. Pitarke, E. V. Chulkov, and V. M. Silkin, J. El. Spec. Rel. Phen. **126**, 163 (2002).

[11] R. W. Schoenlein, J. G. Fujimoto, G. L. Eesley, and T. W. Capehart, Phys. Rev. Lett. **61**, 2596 (1988).

[12] W. Steinmann, Appl. Phys. A **49**, 365 (1989).

[13] R. Fischer, S. Schuppler, N. Fischer, Th. Fauster, and W. Steinmann, Phys. Rev. Lett. **70**, 654 (1993).

[14] B. Quiniou, V. Bulović, and R. M. Osgood, Jr., Phys. Rev. B **47**, 15890 (1993).

[15] Th. Fauster, Prog. Surf. Sci. **46**, 177 (1994).

[16] T. Hertel, E. Knoesel, M. Wolf, and G. Ertl, Phys. Rev. Lett. **76**, 535 (1996).

[17] W. Wallauer and Th. Fauster, Surf. Sci. **374**, 44 (1997).

[18] I. L. Shumay, U. Höfer, Ch. Reuss, U. Thomann, W. Wallauer, and Th. Fauster, Phys. Rev. B **58**, 13974 (1998).

[19] D. Niesner, Th. Fauster, J. I. Dadap, N. Zaki, K. R. Knox, P.-C. Yeh, R. Bhandari, R. M. Osgood, M. Petrović, and M. Kralj, Phys. Rev. B **85**, 081402(R) (2012).

[20]W. R. Merry, R. E. Jordan, D. F. Padowitz, and C. B. Harris, Surf. Sci. **295**, 393 (1993).
[21]Th. Fauster and W. Steinmann, in *Electromagnetic Waves: Recent Developments in Research*, edited by P. Halevi, Vol. 2 (North-Holland, Amsterdam, 1995), Chap. 8, p. 347.
[22]M. Wolf, Surf. Sci. **377–379**, 343 (1997).
[23]C. B. Harris, N.-H. Ge, R. L. Lingle, J. D. McNeill, and C. M. Wong, Annu. Rev. Phys. Chem. **48**, 711 (1997).
[24]T. Munakata and K. Shudo, Surf. Sci. **433–435**, 184 (1999).
[25]Th. Fauster, Ch. Reuss, I. L. Shumay, and M. Weinelt, Chem. Phys. **251**, 111 (2000).
[26]S. Link, H. A. Dürr, G. Bihlmayer, S. Blügel, W. Eberhardt, E. V. Chulkov, V. M. Silkin, and P. M. Echenique, Phys. Rev. B **63**, 115420 (2001).
[27]A. Hotzel, Prog. Surf. Sci. **82**, 336 (2007).
[28]M. Shibuta, K. Miyakubo, T. Yamada, and T. Munakata, J. Phys. Chem. C **115**, 19269 (2011).
[29]P. Szymanski, S. Garrett-Roe, and C. B. Harris, Prog. Surf. Sci. **78**, 1 (2005).
[30]U. Bovensiepen, Prog. Surf. Sci. **78**, 87 (2005).
[31]J. Zhao, B. Li, K. Onda, M. Feng, and H. Petek, Chem. Rev. **106**, 4402 (2006).
[32]J. Stähler, U. Bovensiepen, M. Meyer, and M. Wolf, Chem. Soc. Rev. **37**, 2180 (2008).
[33]H. Petek and J. Zhao, Chem. Rev. **110**, 7082 (2010).
[34]F. Budde, T. F. Heinz, M. M. T. Loy, J. A. Misewich, F. de Rougemont, and H. Zacharias, Phys. Rev. Lett. **66**, 3024 (1991).
[35]Ch. Frischkorn and M. Wolf, Chem. Rev. **106**, 4207 (2006).
[36]W. Wallauer and Th. Fauster, Phys. Rev. B **54**, 5086 (1996).
[37]M. Aeschlimann, M. Bauer, S. Pawlik, W. Weber, R. Burgermeister, D. Oberli, and H. C. Siegmann, Phys. Rev. Lett. **79**, 5158 (1997).
[38]M. Bauer and M. Aeschlimann, J. El. Spec. Rel. Phen. **124**, 225 (2002).
[39]H.-S. Rhie, H. A. Dürr, and W. Eberhardt, Phys. Rev. Lett. **90**, 247201 (2003).
[40]M. Cinchetti, M. Sánchez Albaneda, D. Hoffmann, T. Roth, J.-P. Wüstenberg, M. Krauß, O. Andreyev, H. C. Schneider, M. Bauer, and M. Aeschlimann, Phys. Rev. Lett. **97**, 177201 (2006).
[41]U. Bovensiepen, J. Phys.: Condens. Matter **19**, 083201 (2007).
[42]M. Weinelt, A. B. Schmidt, M. Pickel, and M. Donath, Prog. Surf. Sci. **82**, 388 (2007).
[43]M. Pickel, A. B. Schmidt, M. Weinelt, and M. Donath, Phys. Rev. Lett. **104**, 237204 (2010).
[44]H. C. Schneider, J.-P. Wüstenberg, O. Andreyev, K. Hiebbner, L. Guo, J. Lange, L. Schreiber, B. Beschoten, M. Bauer, and M. Aeschlimann, Phys. Rev. B **73**, 081302(R) (2006).
[45]J.-P. Wüstenberg, M. Cinchetti, M. Sánchez Albaneda, M. Bauer, and M. Aeschlimann, J. Magn. Magn. Mater. **316**, e411 (2007).
[46]W. Nessler, S. Ogawa, H. Nagano, H. Petek, J. Shimoyama, Y. Nakayama, and K. Kishio, Phys. Rev. Lett. **81**, 4480 (1998).
[47]Y. Sonoda and T. Munakata, Phys. Rev. B **70**, 134517 (2004).
[48]R. Cortés, L. Rettig, Y. Yoshida, H. Eisaki, M. Wolf, and U. Bovensiepen, Phys. Rev. Lett. **107**, 097002 (2011).
[49]L. Perfetti, P. A. Loukakos, M. Lisowski, U. Bovensiepen, H. Berger, S. Biermann, P. S. Cornaglia, A. Georges, and M. Wolf, Phys. Rev. Lett. **97**, 067402 (2006).
[50]S. Hellmann, M. Beye, Ch. Sohrt, T. Rohwer, F. Sorgenfrei, H. Redlin, M. Kalläne, M. Marczynski-Bühlow, M. Bauer, A. Föhlisch *et al.*, Phys. Rev. Lett. **105**, 187401 (2010).
[51]F. Schmitt, P. S. Kirchmann, U. Bovensiepen, R. G. Moore, J.-H. Chu, D. H. Lu, L. Rettig, M. Wolf, I. R. Fisher, and Z.-X. Shen, New J. Phys. **13**, 063022 (2011).
[52]T. Rohwer, S. Hellmann, M. Wiesenmayer, Ch. Sohrt, A. Stange, B. Slomski, A. Carr, Y. Liu, L. Miaja-Avila, M. Kalläne *et al.*, Nature (London) **471**, 490 (2011).
[53]J. A. Sobota, S. Yang, J. G. Analytis, Y. L. Chen, I. R. Fisher, P. S. Kirchmann, and Z.-X. Shen, Phys. Rev. Lett. **108**, 117403 (2012).
[54]U. Höfer, I. L. Shumay, Ch. Reuss, U. Thomann, W. Wallauer, and Th. Fauster, Science **277**, 1480 (1997).
[55]U. Höfer, Appl. Phys. B **68**, 383 (1999).
[56]Th. Fauster and M. Weinelt, J. El. Spec. Rel. Phen. **114–116**, 269 (2001).
[57]S. Ogawa, H. Nagano, H. Petek, and A. P. Heberle, Phys. Rev. Lett. **78**, 1339 (1997).
[58]H. Petek, A. P. Heberle, W. Nessler, H. Nagano, S. Kubota, S. Matsunami, N. Moriya, and S. Ogawa, Phys. Rev. Lett. **79**, 4649 (1997).
[59]S. Ogawa, H. Nagano, and H. Petek, Surf. Sci. **427-428**, 34 (1999).
[60]J. Güdde, M. Rohleder, T. Meier, S. W. Koch, and U. Höfer, Science **318**, 1287 (2007).
[61]M. Aeschlimann, M. Bauer, and S. Pawlik, Chem. Phys. **205**, 127 (1996).
[62]S. Pawlik, M. Bauer, and M. Aeschlimann, Surf. Sci. **377–379**, 206 (1997).
[63]E. Knoesel, A. Hotzel, and M. Wolf, J. El. Spec. Rel. Phen. **88–91**, 577 (1998).
[64]Ch. Reuss, I. L. Shumay, U. Thomann, M. Kutschera, M. Weinelt, Th. Fauster, and U. Höfer, Phys. Rev. Lett. **82**, 153 (1999).
[65]H. Petek, H. Nagano, and S. Ogawa, Phys. Rev. Lett. **83**, 832 (1999).
[66]M. Aeschlimann, M. Bauer, S. Pawlik, R. Knorren, G. Bouzerar, and K. H. Bennemann, Appl. Phys. A **71**, 485 (2000).
[67]M. Weinelt, J. Phys.: Condens. Matter **14**, R1099 (2002).
[68]X. J. Shen, H. Kwak, A. M. Radojevic, S. Smadici, D. Mocuta, and R. M. Osgood, Jr., Chem. Phys. Lett. **351**, 1 (2002).
[69]W. Berthold, U. Höfer, P. Feulner, E. V. Chulkov, V. M. Silkin, and P. M. Echenique, Phys. Rev. Lett. **88**, 056805 (2002).
[70]P. M. Echenique, R. Berndt, E. V. Chulkov, Th. Fauster, A. Goldmann, and U. Höfer, Surf. Sci. Rep. **52**, 219 (2004).
[71]S. Garrett-Roe, S. T. Shipman, P. Szymanski, M. L. Strader, A. Yang, and C. B. Harris, J. Phys. Chem. B **109**, 20370 (2005).
[72]Th. Fauster, M. Weinelt, and U. Höfer, Prog. Surf. Sci. **82**, 224 (2007).
[73]B. Gumhalter, A. Šiber, H. Buljan, and Th. Fauster, Phys. Rev. B **78**, 155410 (2008).
[74]E. V. Chulkov, I. Sarría, V. M. Silkin, J. M. Pitarke, and P. M. Echenique, Phys. Rev. Lett. **80**, 4947 (1998).
[75]P. M. Echenique, J. M. Pitarke, E. V. Chulkov, and A. Rubio, Chem. Phys. **251**, 1 (2000).
[76]V. P. Zhukov, O. Andreyev, D. Hoffmann, M. Bauer, M. Aeschlimann, E. V. Chulkov, and P. M. Echenique, Phys. Rev. B **70**, 233106 (2004).
[77]P. S. Kirchmann, L. Rettig, X. Zubizarreta, V. M. Silkin, E. V. Chulkov, and U. Bovensiepen, Nat. Phys. **6**, 782 (2010).
[78]R. Knorren, G. Bouzerar, and K. H. Bennemann, Phys. Rev. B **63**, 125122 (2001).

[79]S. Ramakrishna, F. Willig, and A. Knorr, Appl. Phys. A **78**, 247 (2004).
[80]A. Zeiser, N. Bücking, J. Förstner, and A. Knorr, Phys. Rev. B **71**, 245309 (2005).
[81]B. Rethfeld, A. Kaiser, M. Vicanek, and G. Simon, Phys. Rev. B **65**, 214303 (2002).
[82]C. Timm and K. H. Bennemann, J. Phys.: Condens. Matter **16**, 661 (2004).
[83]H. Ueba and T. Mii, Appl. Phys. A **71**, 537 (2000).
[84]M. Sakaue, H. Kasai, and A. Okiji, J. Phys. Soc. Jpn. **69**, 160 (2000).
[85]M. Sakaue, T. Munakata, H. Kasai, and A. Okiji, Phys. Rev. B **66**, 094302 (2002).
[86]M. Sakaue, J. Phys.: Condens. Matter **17**, S245 (2005).
[87]W. Schattke, E. E. Krasovskii, R. Díez Muiño, and P. M. Echenique, Phys. Rev. B **78**, 155314 (2008).
[88]Zhaofeng Hao, J. I. Dadap, K. R. Knox, M. B. Yilmaz, N. Zaki, P. D. Johnson, and R. M. Osgood, Jr., Phys. Rev. Lett. **105**, 017602 (2010).
[89]K. I. Shudo and T. Munakata, Phys. Rev. B **63**, 125324 (2001).
[90]C. Kentsch, M. Kutschera, M. Weinelt, Th. Fauster, and M. Rohlfing, Phys. Rev. B **65**, 035323 (2001).
[91]M. Kutschera, M. Weinelt, M. Rohlfing, and Th. Fauster, Appl. Phys. A **88**, 519 (2007).
[92]M. Weinelt, M. Kutschera, Th. Fauster, and M. Rohlfing, Phys. Rev. Lett. **92**, 126801 (2004).
[93]S. Jeong, H. Zacharias, and J. Bokor, Phys. Rev. B **54**, R17300 (1996).
[94]S. Tanaka and K. Tanimura, Phys. Rev. B **77**, 195323 (2008).
[95]M. Weinelt, M. Kutschera, R. Schmidt, Ch. Orth, Th. Fauster, and M. Rohlfing, Appl. Phys. A **80**, 995 (2005).
[96]T. Ichibayashi and K. Tanimura, Phys. Rev. Lett. **102**, 087403 (2009).
[97]T. Ichibayashi, S. Tanaka, J. Kanasaki, K. Tanimura, and Th. Fauster, Phys. Rev. B **84**, 235210 (2011).
[98]Ch. Eickhoff, M. Teichmann, and M. Weinelt, Phys. Rev. Lett. **107**, 176804 (2011).
[99]Th. Fauster, S. Tanaka, and K. Tanimura, Phys. Rev. B **84**, 235444 (2011).
[100]H. Husser, J. van Heys, and E. Pehlke, Phys. Rev. B **84**, 235135 (2011).
[101]M. Bockstedte, A. Kley, J. Neugebauer, and M. Scheffler, Comput. Phys. Commun. **107**, 187 (1997).
[102]L. Kleinman and D. M. Bylander, Phys. Rev. Lett. **48**, 1425 (1982).
[103]In the present simulation of surface normal emission, the gauge factors to the valence band projector have been omitted. This corresponds to setting the periodic parts of the Kohn-Sham wave functions constant in the neighborhood of the $\overline{\Gamma}$ point.
[104]S. Ismail-Beigi, E. K. Chang, and S. G. Louie, Phys. Rev. Lett. **87**, 087402 (2001).
[105]W. C. Henneberger, Phys. Rev. Lett. **21**, 838 (1968).
[106]R. Schlier and H. Farnsworth, J. Chem. Phys. **30**, 917 (1959).
[107]D. J. Chadi, Phys. Rev. Lett. **43**, 43 (1979).
[108]A. Ramstad, G. Brocks, and P. J. Kelly, Phys. Rev. B **51**, 14504 (1995).
[109]J. E. Northrup, Phys. Rev. B **47**, 10032 (1993).
[110]P. Krüger and J. Pollmann, Phys. Rev. Lett. **74**, 1155 (1995).
[111]W. Brenig and E. Pehlke, Prog. Surf. Sci. **83**, 263 (2008).
[112]J. van Heys, M. Lindenblatt, and E. Pehlke, Phase Transitions **78**, 773 (2005).
[113]A. Fleszar and W. Hanke, Phys. Rev. B **56**, 10228 (1997).
[114]M. Wolf, A. Hotzel, E. Knoesel, and D. Velic, Phys. Rev. B **59**, 5926 (1999).
[115]M. Wagner, *Gruppentheoretische Methoden in der Physik* (Vieweg, Braunschweig, 1998).
[116]The term proportional to $\hat{\mathbf{A}}^2$ is omitted in the dipole approximation. The gauging of the nonlocal potentials introduces further terms (of the form $\hat{V}_{\mathrm{nl}}^{\mathbf{A}} - \hat{V}_{\mathrm{nl}}^{\mathbf{0}}$) to the interaction operator that have been neglected here.
[117]W. Schattke and M. A. van Hove (eds.), *Solid-State Photoemission and Related Methods. Theory and Experiment* (Wiley-VCH, Weinheim, 2003).
[118]Whenever the same IS structure is present in both single-domain spectra (s_X and s_Y or p_X and p_Y), the corresponding peak positions may slightly differ and have to be redetermined in the averaged two-domain spectra—this accounts for the minor variations of peak positions in the respective spectra.
[119]The energies determined by this equation are consistent with the energies of the IS known from the decomposition of the spectra within the tolerance introduced by the finite energy width of the laser pulse.
[120]The time-dependent Kohn-Sham wave functions carry information on different excitations including the polarization of the system (of first order with respect to the external field) and the losses due to inelastic scattering in the excited states. To extract the contribution of an unoccupied state to the 2PPE spectrum it is desirable to make explicit use of the matrix elements with the final-state wave functions.
[121]Note that in such a case, also the relative phases of the second transition to the FS might vary with photon energy which may give rise to a FS phase effect—in contrast to the FS effect of Fig. 10 that rests solely on the strength of the transition.
[122]The states are discretized in the finite slab calculation and separated by ≈200 meV in energy in the case of $\Delta_{2'}$.
[123]Th. Fauster, in *Solid-State Photoemission and Related Methods. Theory and Experiment*, edited by W. Schattke and M. A. van Hove (Wiley-VCH, Weinheim, 2003), Chap. 8, p. 247.
[124]J. Pollmann, R. Kalla, P. Krüger, A. Mazur, and G. Wolfgarten, Appl. Phys. A **41**, 21 (1986).